Catalysis and Surface Science: What Do We Learn from Studies of Oxide-Supported Cluster Model Systems?

H.-J. FREUND, M. BÄUMER, AND H. KUHLENBECK

Fritz-Haber-Institut der Max-Planck-Gesellschaft
Department of Chemical Physics
D-14195 Berlin, Germany

Models of supported metal catalysts have been prepared by deposition of transition metal vapor onto thin, well-ordered oxide layers, particularly alumina. The average sizes of the metal particles and their size distributions are determined by nucleation and growth. Here, we review the morphology and structure of the oxide layers and the metal particles dispersed on them, as measured with a variety of methods including low-energy electron diffraction and scanning tunneling microscopy. Electronic and magnetic structure as a function of particle size, adsorption properties, as well as reactivity with varying particle size are reviewed. The electronic structure of supported palladium particles has been studied and indicates that a nonmetal to metal transition occurs for particles exceeding 70–80 atoms per aggregate. Adsorption of CO has been studied in detail by Fourier transform infrared spectroscopy. Interesting variations in the spectra when very small particles consisting of only a few metal atoms are investigated compared with larger particles and single-crystal surfaces are observed. CO dissociation has been studied on rhodium aggregates and a maximal dissociation rate has been found for aggregates containing several hundred metal atoms. The presence of defects on the particles is deduced to be origin of this behavior.

Abbreviations: AFM, atomic force microscopy; EEL, electron energy loss; EELS, electron energy loss spectroscopy; EL, electron loss; FFT, fast Fourier transform; FMR, ferro-magnetic resonance; FT, Fourier-transform; FTIR, Fourier transform infrared; GIXD, grazing incidence X-ray diffraction; HRTEM, high resolution transmission electron microscopy; IR, infrared; LEED, low energy electron diffraction; ML, mono-layer; RAIRS, reflection absorption infrared spectroscopy; SFG, sum frequency generation; SPA-LEED, spot profile analysis-low energy electron diffraction; STM, scanning tunneling microscopy; TDS, thermal desorption spectroscopy; TEM, transmission electron microscopy; UHV, ultrahigh vacuum; XP, X-ray photoelectron; XPS, X-ray photoelectron spectroscopy.

I. Introduction

From its beginning, surface science has largely been driven by the goal of understanding catalysis at the atomic level, with more recent work being motivated by the goals of understanding microelectronic and sensor materials and phenomena such as corrosion (*1, 2*).

Adsorbates on metal single-crystal surfaces have been characterized with the aim of demonstrating some of the basic mechanisms of catalysis, e.g., how small molecules such as H_2, CO, NO, CO_2, and N_2 interact with structurally well-characterized surfaces, how the electronic and geometric structures of these molecules and the surface are changed as a result of the adsorbate–surface interactions, and how these interactions open pathways for reaction of the adsorbates with coadsorbed species. With the development of an arsenal of surface analytical tools, the past 35 years of surface science have witnessed major progress, although some of the early claims were unrealistic and much remains to be understood. Catalysis remains a strong driving force for surface science (*2*), and it is vital that the catalysis and surface science communities continue to interact with the goal of eventually being united.

The gaps that still exist between catalysis and surface science (*3*) were identified early (4):

1. The materials gap
2. The pressure gap
3. The complexity gap

Surface science has reached a degree of maturity that should allow us to bridge these gaps (*5–17*). The use of model systems (*16*), including model catalysts, is one strategy for bridging the materials and pressure gaps. We believe that these two gaps have to be bridged before the complexity gap can be bridged.

A wide variety of systems serve as models of practical catalysts. Reviews that deal particularly with models of dispersed metal or dispersed metal oxide catalysts include those by Goodman (*11*), Niemantsverdriet *et al.* (*16*), and our group (*10, 13*). Although the approaches to preparation of models of practical supported catalysts have much in common, there are some subtle and important differences among them.

Briefly, the various approaches share the requirement that the substrate onto which the model is built should be electrically conducting to allow application of the appropriate surface science tools, as shown in Fig. 1 (*3, 10, 11, 16, 17*). The catalyst support is prepared on these substrates as a thin layer because most practical supports, such as magnesia, alumina, or silica, are insulators. When they are sufficiently thin, these layers are

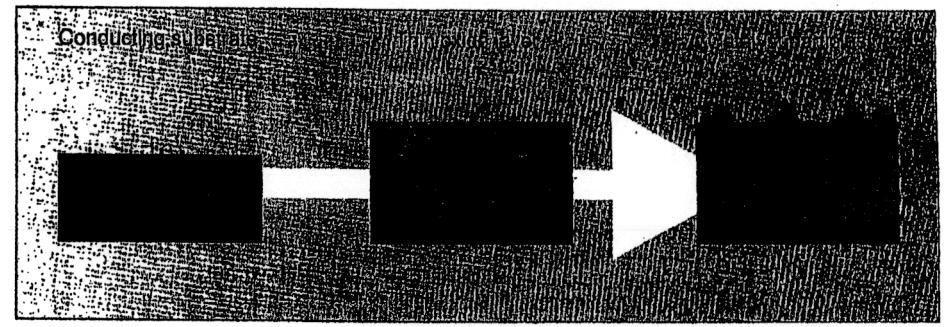

FIG. 1. Schematic diagram of model catalyst systems.

sufficiently conductive to allow application of analytical methods based on sample interrogation with charged particles without severe charging of the sample.

The active catalyst phase is deposited on the support, which is often an oxide. This catalyst phase may consist of aggregates of metal or, alternatively, a second oxide, a carbide, or a nitride, prepared in dispersed form.

Oxide supports are emphasized in this review. The model supports are prepared in various ways. Oxide layers can be grown as native oxides on metals (*3, 9*). In this case, the structure is governed by the natural mismatch of the structures of the metal and its oxide; sometimes the resulting layers are well structured and sometimes they are amorphous. Oxide layers may also be grown by evaporation of the metal onto a second (inert) metal substrate (*11*). The structure of the metal then largely governs the structural quality of the layer. Again, ordered or amorphous layers can be grown. Oxidation can be carried out by evaporation of the metal in an oxygen atmosphere or by exposing the deposited metal layer to oxygen in a second step (*15*). The morphology of the oxide layer may depend critically on the preparation procedure.

Films of carbides (*18*), nitrides (*19*), or sulfides (*20*) can be prepared similarly if a good method for providing the nonmetallic element is known. It is obvious that if the support is conductive (a conductive oxide or graphite), single crystals (*21*) of the respective materials may be used as well.

A variety of methods have been applied for depositing the active catalytic material in a second step. The most popular involves evaporation of the metal. If the deposition rate and the substrate temperature are controlled, then relatively narrow metal particle size distributions can be obtained, and the metal loading can be varied (*10*). Deposition of mass-selected

particles may emerge as the preferred method to control particle size for the smallest aggregates (*22*). Chemical vapor deposition of cluster compounds or of organometallic compounds is another possibility (*23*). When these precursors are used, it is usually important to ensure that the ligands do not remain as permanent contaminants of the aggregates.

Additional preparation methods include wet impregnation spin coating (*16*), whereby the precursor of the active component is brought onto the support in solution. The solvent is evaporated and then the precursor is further treated to give the active form.

Although it seems that all the methods yield model systems which are "cum grano solis" the same, there are fundamental differences between the wet impregnation techniques on microcrystalline layers and those involving growth of particles by metal vapor deposition onto single-crystal supports, for example. The first (top-down) approach, although similar to industrially employed catalyst preparation procedures, is characterized by complex processes. The second (bottom-up) approach, on the other hand, starts almost from first principles and tries to be as rigorous as possible in each step of increasing complexity. The bottom-up approach, however, sometimes leads those in the catalysis community to question the relevance of the materials to practical catalysis; one may ask whether the model system has been tested in a catalytic reaction and whether it is active for the reaction it is intended to model. If the answers are negative, then the top-down approach is favored. It can be argued, however, that although the complex model system may do what it is supposed to, its complexity may stymie understanding of the underlying atomic-scale phenomena, which may be more easily isolated by the bottom-up approach.

Microcrystalline powders may also serve as model systems (which are not directly compatible with Fig. 1) that are well-suited for comparison with those made by the bottom-up approach described previously. The groups of Knözinger (*24*) and Zecchina *et al.* (*25*) have made seminal contributions to this area by their infared (IR) and Raman spectroscopic studies of adsorbed probe molecules. If grown and sintered properly, the microcrystals expose single-crystal facets. The adsorption sites on the various facets and possibly on edge and corner sites can be differentiated by the adsorption of probe molecules, the internal mode frequencies of which depend on the adsorption site. Assignment of some of the frequencies by comparison of spectra with those characterizing large single-crystal samples is a first step toward accounting for the complex set of adsorption sites. The complementary nature of the results characterizing microcrystalline and single-crystal materials is helping to close the materials gap (*26*).

Closing the pressure gap can be achieved by application of surface-sensitive techniques that work in the presence of a gas phase, such as thermal desorption spectroscopy (TDS), reflection absorption infrared spectroscopy (RAIRS), sum frequency generation (SFG), scanning tunneling microscopy (STM), and X-ray scattering or X-ray absorption (*27*). Closing the full complexity gap must involve the application of additional methods to characterize the gas phase and mass transport.

Our goal in the following review is to describe the bottom-up approach and provide examples illustrating how far surface science has progressed and what may possibly be accomplished in the near future.

II. Clean Oxide Surfaces: Structure and Adsorption

The preparation of a clean oxide surface is difficult; several strategies have been proposed (*5, 15, 21*). The most straightforward is ultrahigh vacuum is (UHV) *in situ* cleavage, which leads to good results only in certain cases, such as for MgO, NiO, ZnO, and $SrTiO_3$ (*9*). Some catalytically important oxides, such as Al_2O_3, SiO_2, and TiO_2, are difficult to cleave (*21*). A disadvantage encountered in experimental investigations of cleaved bulk single-crystal insulators is the sample charging that results when they are bombarded by charged particles, as in electron spectroscopy experiments. An alternative method of preparing bulk single crystals of oxides is *ex situ* cutting and polishing followed by *in situ* sputtering and subsequent annealing in oxygen. Such a process usually creates a sufficient number of defect sites in the near-surface region and in the bulk to induce conductivity of the material. Thus, electron spectroscopies and STM can be applied (*21*).

Single-crystal oxide surfaces may also be prepared by the growth of thin oxide layers on single-crystal metal supports (*5, 13, 15*). All the surface science tools can be applied to such samples. If the oxide layer is to represent the bulk accurately, care must be taken to provide the proper layer thickness. Furthermore, if adsorption and reactivity investigations are intended, the continuity of the layer must be guaranteed. Several examples illustrate the successful attainment of these goals (*11, 13, 16*).

The best studied clean oxide surfaces are $TiO_2(100)$ and $TiO_2(110)$ (*5, 17, 21*). An STM image of the clean (1×1) $TiO_2(110)$ surface taken by Diebold *et al.* (*28*) is shown in Fig. 2. It is noteworthy that one of the first atomically resolved images of this surface was reported by Murray *et al.* (*29, 30*). The inset shows a ball-and-stick model of the surface. Evidence accumulating from theoretical modeling of the tunneling conditions and from adsorbate studies using molecules assumed to bind to the exposed titanium sites indicates that the bright rows represent titanium atoms. Onishi *et al.* (*31–34*) used formic acid in such an investigation and showed, in line with the theoretical predictions (but in contrast to intuitive expectations

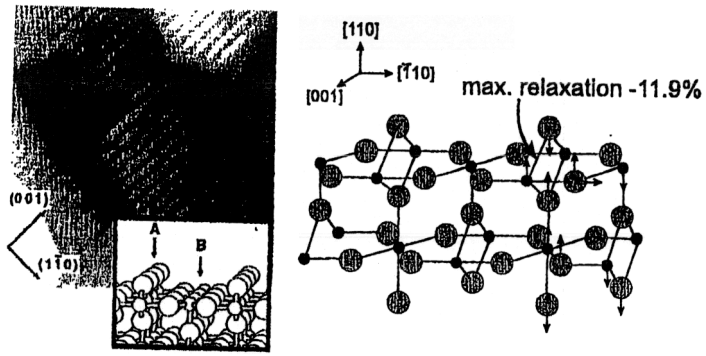

FIG. 2. Structure of the TiO_2(110) surface as determined by STM (left) and grazing incidence X-ray scattering (right). The groups of Bonnell, Diebold, Iwasawa, Thornton, and Vanderbilt contributed to the solution of this problem [reproduced with permission from Diebold *et al.* (*28*) (left) and Charlton *et al.* (*35*) (right)].

based on topological arguments), that the titanium atoms are imaged as bright lines and the oxygen atoms as dark lines. Taking account of the resolvable interatomic distances within the surface layer, the authors inferred that the values correspond to the structure of the neutral truncation of the stoichiometric (110) surface (*35, 36*). Interatomic distances normal to the surface, however, differ substantially from the bulk values, as shown by X-ray scattering experiments. The top-layer, sixfold coordinated titanium atoms move outward and the fivefold coordinated titanium atoms move inward, leading to a surface roughening of 0.3 ± 0.1 Å. The roughening repeats itself in the second layer with an amplitude about half of that in the top layer. Bond length variations range from a contraction of 11.3% to an expansion of 9.3%. These strong relaxations are not atypical for oxide surfaces and have been predicted theoretically (*37–39*).

The relaxations are particularly pronounced for the so-called charge-neutralized polar surfaces (*37–39*). There are several experimental results (*40–43*) that essentially corroborate the theoretical predictions, although the quantitative agreement is not always good (*44–47*). Specifically, the (0001) surfaces of corundum-type materials, such as Al_2O_3 (*44, 45*), Cr_2O_3 (*46*), and Fe_2O_3 (*47*), have been investigated with X-ray diffraction, quantitative low-energy electron diffraction (LEED), STM, and theory.

Figure 3 (*48, 49*) is a reminder that a polar surface [e.g., the (111) orientation of a rock salt structure] exhibits, when the bulk is terminated, a diverging surface potential due to the missing compensation of the interlayer dipole moments, as discussed by Noguera (*39*). Consequently, polar surfaces reconstruct and/or relax substantially, whereas nonpolar surfaces often

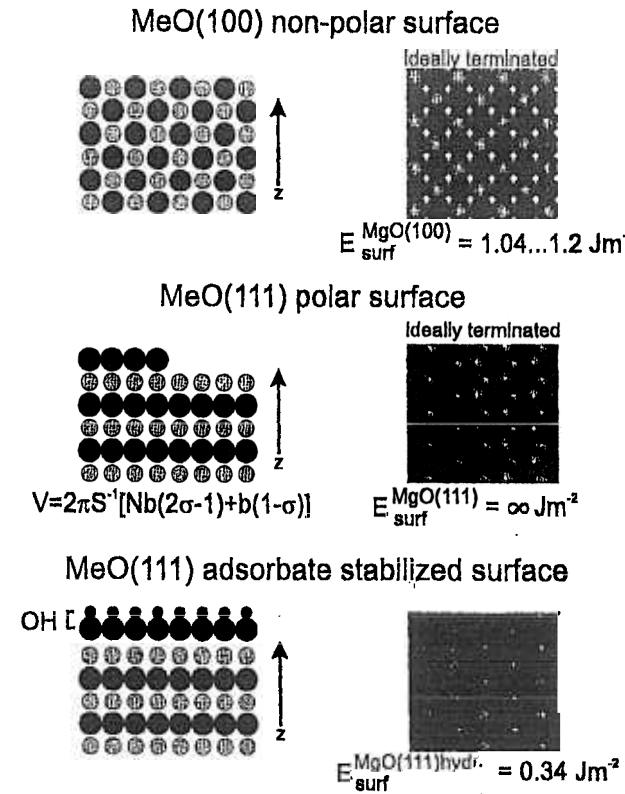

FIG. 3. Schematic representation (side and top views) of the structure of a nonpolar (top) an unreconstructed polar (middle), and a hydroxylated polar (bottom) surface of a rock salt-type crystal. The energies given refer to MgO (*48*).

exhibit much less pronounced relaxations (although, as was shown previously for TiO_2, the degree of relaxation might still be substantial).

Figure 4 shows the results of structural determinations for the three related systems Al_2O_3(0001), Cr_2O_3(0001), and Fe_2O_3(0001). In all three, a stable structure is given by the metal ion-terminated surface retaining only half the number of metal ions in the surface relative to a full buckled layer of metal ions within the bulk. The interlayer distances are strongly relaxed, with the relaxation extending several layers below the surface. The perturbation to the structure caused by the presence of the surface in oxides is considerably more pronounced than in metals, for which the interlayer relaxations are typically on the order of a few percent (*50*). The absence of the screening charge in a dielectric material such as an oxide contributes

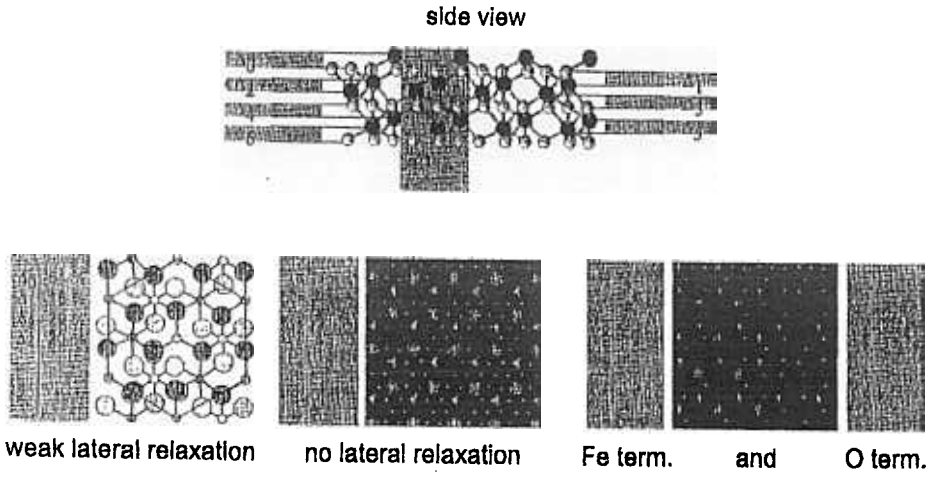

FIG. 4. Experimental results characterizing the structure of corundum-type depolarized (0001) surfaces (side and top views) [reproduced with permission from Renaud (*36*) (left), Rohr *et al.* (*42*) (middle), and Wang *et al.* (*47*) (right)].

significantly to this effect. It has recently been pointed out (*51*) that oxide structures may not be as rigid as has been previously thought on the basis of the relatively stiff phonon spectrum of the bulk. Indeed, at the surface the phonon spectrum may become soft so that the geometric structure becomes flexible and thus significantly dependent on the presence of adsorbed species.

Bulk oxide stoichiometries depend strongly on oxygen pressure (*52*). Both the stoichiometries and the structures of oxide surfaces depend on the oxygen pressure, as illustrated by a recent investigation of the $Fe_2O_3(0001)$ surface (*47*). If a Fe_2O_3 single-crystal layer is grown at a low oxygen pressure, the surface is metal terminated, whereas growth under higher oxygen pressures leads to a complete oxygen termination (*47*). In principle, this surface would be regarded as unstable on the basis of the electrostatic arguments presented previously. However, calculations (*47*) have shown that a strong rearrangement of the electron distribution, as well as relaxation between the layers, leads to a stabilization of the system. STM images (*47*) corroborate the coexistence of oxygen- and iron-terminated layers and thus indicate that stabilization must occur.

Of course, additional structural characterization is needed. The idea of polar and nonpolar surfaces only really holds in its simplest version if the material is highly ionic. Thus, the most extreme cases to investigate are perhaps the polar surfaces of the simple oxides with the rock salt structure

(*53*), such as MgO and NiO [i.e., MgO(111) and NiO(111)]. Barbier and Renaud (*54*) succeeded in preparing a single-crystal NiO(111) surface and in characterizing it by grazing-incidence X-ray diffraction (GIXD). As was shown earlier for thin NiO layers of different crystallographic orientations [i.e., NiO(100) (*55*) and NiO(111) (*56*)], a surface prepared in air or under residual gas pressure exhibits a $p(1 \times 1)$ structure, whereas the clean polar (111) surfaces are reconstructed. The $p(2 \times 2)$ reconstruction originally reported for the thin layer system has also been found for the bulk single-crystal surfaces (*53, 54*). An initial structural analysis suggested that the structure is not the expected octopolar reconstruction shown in Fig. 5 but instead a more complicated one (*53*). However, recent investigations (*57*) of more carefully prepared bulk single-crystal surfaces revealed that a stoichiometric surface actually reconstructs according to the octopolar scheme (*39, 58*). The small (100)-terminated pyramids are oxygen terminated.

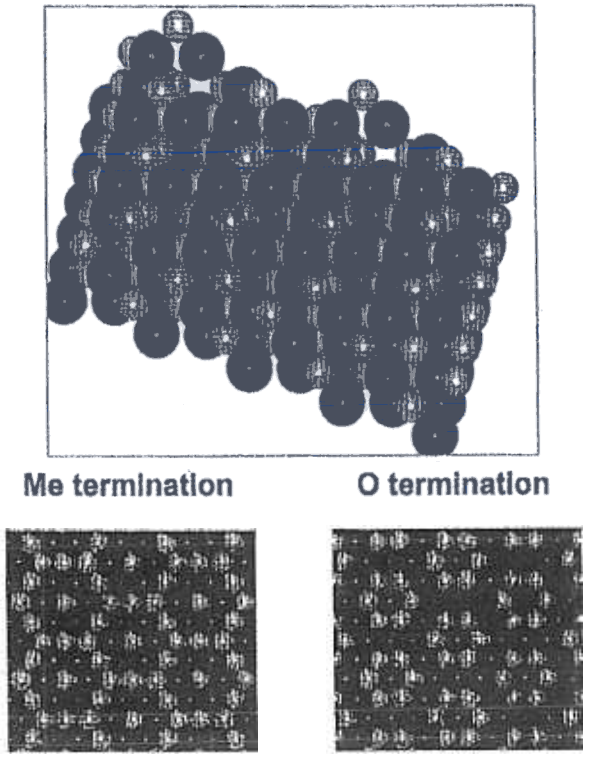

FIG. 5. Schematic representation of the octopolar reconstruction of a polar rock salt (111) surface with oxygen and metal termination [reproduced with permission from Wolf (*53*)].

Furthermore, NiO(111) layers grown on Au(111) which were initially studied by Ventrice *et al.* (*59*) have recently been investigated by GIXD (*60*). The p(2 × 2) reconstruction was again corroborated, but the structural analyses undertaken to date seem to favor a structure in which oxygen as well as Ni-terminated octopoles, possibly arranged on adjacent terraces, constitute the surface layer. Both the bulk single-crystal surfaces and the NiO(111) layer surfaces grown on Au(111) exhibit a high degree of surface order. This is probably one reason why these surfaces do not quickly restructure upon exposure to water, whereas NiO(111) layers grown on Ni(111) do reconstruct to form a hydroxyl-terminated NiO(111) surface (*56*). A microscopic mechanism would involve massive material transport across the surface, which is less favorable on more ordered surfaces and may therefore be kinetically hindered on well-ordered single crystals.

The interaction of water with polar oxide surfaces is a topic of general interest in geochemical and environmental science (*61*) as well as in catalysis. With respect to the latter, Papp and Egersdörfer (*62*) and Egersdörfer (*63*) found indications that NiO catalysts prepared with preferential (111) crystallographic orientation by topotactical dehydration of $Ni(OH)_2$ show the highest activity for deNO_x reactions after the last monolayer of H_2O has been desorbed. Even in 1977, Fripiat *et al.* (*64*) showed theoretically on the basis of energetic considerations that real crystallites must be terminated partly by polar surfaces the charges of which are reduced by surface OH groups.

Thus, the interactions of molecules with oxide surfaces represent an important field. In the following, we discuss several examples illustrating aspects of the bonding and interaction of molecules with oxide surfaces and, for comparison, metal surfaces.

The bonding of molecules to oxides is different from the bonding of molecules to metals. For example, a CO molecule interacts with metals via chemical bonds of varying strengths involving charge transfer (*65*). Figure 6 schematically illustrates the bonding of CO to a Ni metal atom by σ donation/π back-donation on the basis of a one-electron orbital diagram. The σ and π interactions lead to a shift of those σ and π orbitals involved in the bond with respect to those orbitals not involved. The diagram reflects this shift with the correlation lines.

This bonding of CO to a metal is in contrast to the electrostatically dominated interaction between a CO molecule and a nickel ion in nickel oxide (*66, 67*). There is a noticeable σ repulsion between the CO carbon lone pair and the oxide, leading to a similar shift of the CO 5σ orbital as in the case of the metal atom. However, there is little or no π back-donation so that the CO π orbitals are not modified (*13, 68*). Conceptually, the situation is transparent, and it might be expected that a detailed calculation

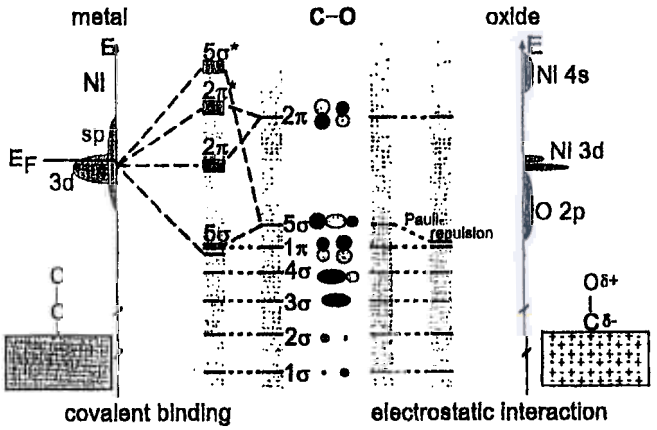

FIG. 6. Orbital diagram for the bonding of CO to nickel metal (left) and to nickel oxide (right).

would reveal the differences quantitatively. However, the description by *ab initio* calculations is rather involved, and a full interpretation cannot be given (*69*). The theoretical prediction is that CO (or NO) binds very weakly to NiO (*69*). The calculated binding energy of CO is on the order of 0.1 eV and expected to be similar to that characterizing CO bonded to MgO(100), i.e., the influence of the nickel d electrons is expected to be negligible (*69*).

To shed light on this problem, thermal desorption measurements were made to characterize cleaved single-crystal surfaces, which are the surfaces with the least number of defects (*70*). In Figs. 7 and 8, TDS data for CO and NO on vacuum-cleaved NiO(100) are compared with data for thin NiO(100) layers grown by oxidation of Ni(100). At temperatures of 30 and 56 K, multilayer desorption of CO and NO, respectively, occurs. The pronounced features at higher temperatures correspond to desorption of the respective adsorbate at (sub)monolayer coverage. In the case of CO, desorption of the second layer occurs at 34 K. The states at 45 and 145 K for CO and NO, respectively, are due to adsorption on defects, as concluded from data obtained with ion-bombarded surfaces (not shown).

For both adsorbates, the thin layer data and the data characterizing the cleaved samples agree well. In particular, for NiO(100) the thin layer data are comparable to those characterizing the more perfect surfaces of the cleaved samples. The higher defect density of the thin layer surfaces leads to small, but clearly visible, additional peaks in the TDS data which, for example, are visible as shoulders near the main peak in the NO spectra.

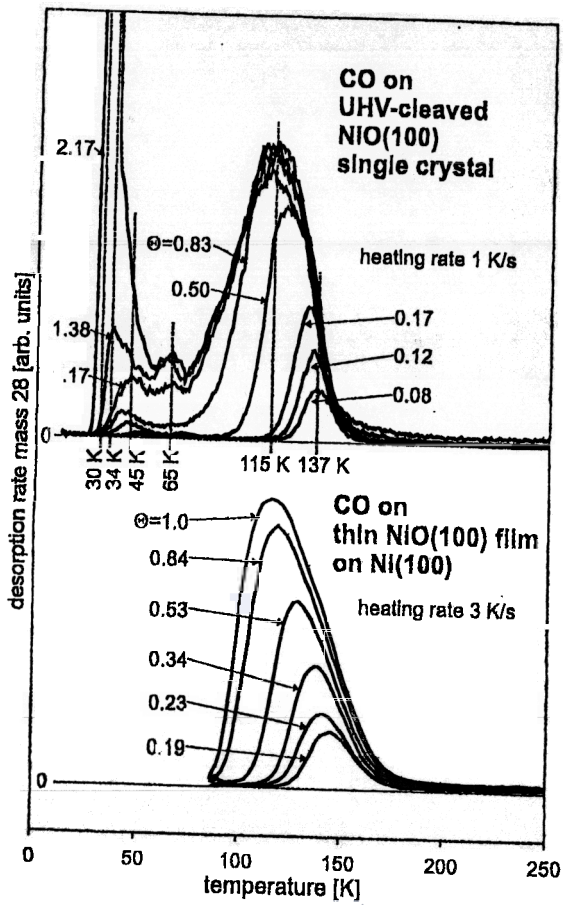

FIG. 7. Thermal desorption spectra of CO on NiO(100) cleaved in vacuum (top) and on a thin NiO(100) layer grown by oxidation of Ni(100) (bottom). The mass spectrometer was set to mass 28 (CO). CO coverages are given relative to full monolayer coverage.

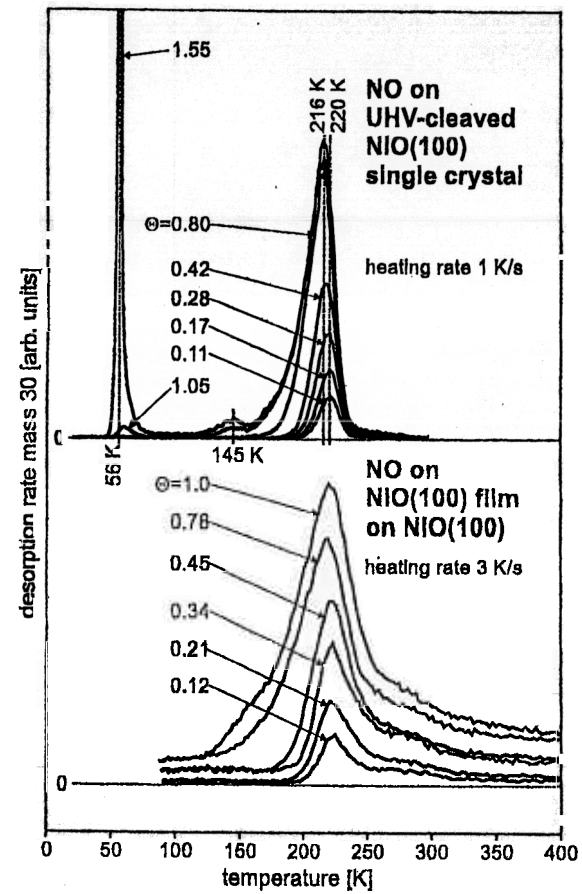

FIG. 8. Thermal desorption spectra of NO on NiO(100) cleaved in vacuum (top) and NO on a thin NiO(100) layer grown by oxidation of Ni(100) (bottom). The mass spectrometer was set to mass 30 (NO). NO coverages are given relative to full monolayer coverage.

Nevertheless, the overall shapes of the thin layer spectra of both adsorbates are very similar to those of the cleaved samples.

The low-coverage adsorption energies representing CO and NO on NiO(100) and MgO(100) are compiled in Table I. According to theory, the interactions of the adsorbates with MgO(100) and NiO(100) are expected to be similar since the bonding should be mainly electrostatic in nature (*69*) [the electric fields at the surfaces of NiO(100) and MgO(100) are similar]. According to Table I, however, the bonding energies are considerably different, with the higher values being obtained for NiO(100). Covalent interactions involving the nickel 3d electron (which have not become evident in the calculations so far) may play a role in the adsorbate–substrate interaction.

The adsorption of CO on MgO has been investigated thoroughly by Heidberg *et al.* (*71*) with IR spectroscopy and by Weiss *et al.* (*72*) with helium atom scattering. They demonstrated clearly that CO forms ordered phases on the cleavage planes and that order and spectroscopic properties depend on the quality of the prepared surfaces. The influence of the presence of surface defects on adsorption properties is obvious from the data,

TABLE I
Compilation of Low-Coverage Bonding Energies for NO and CO on NiO(100) and MgO(100)[a]

CO	0.30 eV	0.14 eV
NO	0.57 eV	0.22 eV

[a] From Wichtendahl *et al.* (*70*)

but a quantitative evaluation based on the number and the nature of the defects has not been reported.

The quantitative evaluation of defects is a well-defined but difficult problem that awaits future investigations. Water adsorption is an example that lends itself to a study of the influence of defects because, at lower coverages, the (100) cleavage planes of MgO or of NiO do not dissociate water, whereas defects induce water dissociation, as is evident in the TDS spectra of H_2O from (100) rock salt-type surfaces. Figure 9 shows results for H_2O desorption from MgO(100) and NiO(100) (*73*). The most pronounced features in the spectra are due to condensed water layers at the lowest desorption temperature and the conversion of a compact layer [with c(2 × 4) periodicity in the case of MgO] to the monolayer, which desorbs at 225 K for MgO(100) and at 240 K for NiO (*74, 75*). The difference in desorption temperature between MgO(100) and NiO(100) seems to be characteristic of the H_2O–substrate interaction.

Most of the TDS information is lost when defects are created by sputtering. Thermal desorption is observed up to relatively high temperatures and the features are broad. Which kinds of defects have been created and how many are not known. A combination of techniques to characterize the defects by probe molecule adsorption together with IR, electron spin resonance, and electron spectroscopies may lead to a deeper understanding in the future.

Dissociative adsorption of water on oxide surfaces can also be used in a preparative way, namely, to modify the surface by hydroxylation. We have used this technique for a thin alumina layer to investigate the influence of hydroxyl groups on the nucleation and growth of metal aggregates, as discussed later (*76*). Figure 10 shows the result of such a hydroxylation as measured with vibrational spectroscopies such as high-resolution electron energy loss spectroscopy and Fourier transform infrared (FTIR) spectroscopy (*77*). It is impossible to hydroxylate the thin alumina layer on NiAl(110) just by water dissociation, whereas on a similar layer grown on

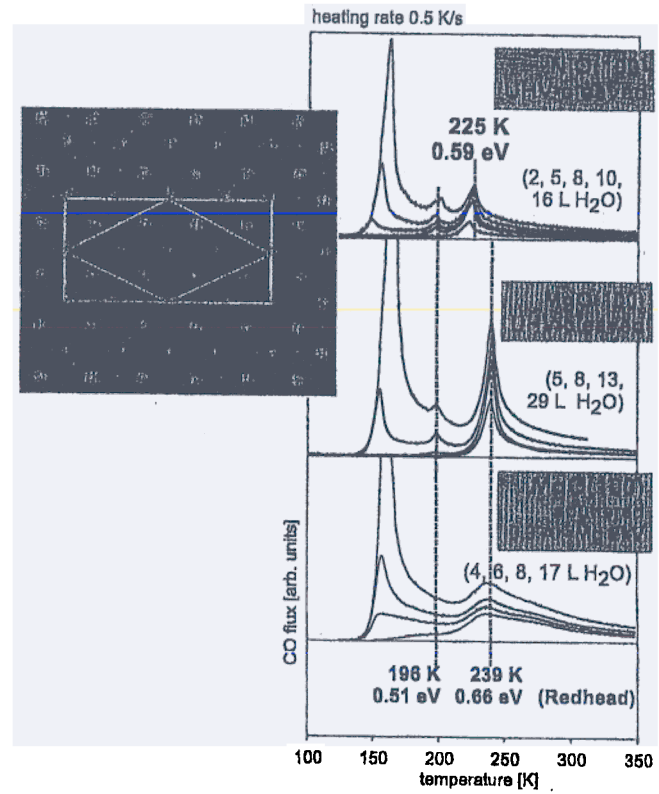

FIG. 9. Thermal desorption spectra of H_2O on UHV-cleaved MgO(100) and NiO(100). A schematic representation of the c(4 × 2) structure is included [reproduced with permission from Heidberg *et al.* (*199*)]. For comparison, a thermal desorption spectrum of MgO(100) taken after creation of defects via sputtering is shown.

NiAl(100) (*78*) formation of OH from dissociative H_2O adsorption occurs. The clean oxide layer surface was exposed to aluminum metal and then the aluminum was hydrolyzed by water adsorption to form a hydroxyl overlayer (*76, 77*). In Fig. 10 (bottom), an electron energy loss spectrum showing the hydroxyl vibration at 465 meV (3750 cm^{-1}) as well as a corresponding spectrum of the clean layer are plotted. The peaks at energies below 120 meV indicate the alumina phonons (*79*), which are broadened by hydroxylation as a result of a change of the surface order. The observed hydroxyl loss coincides clearly with the IR absorption observed for the same sample. In this case, more water was adsorbed so that a broad band from water clusters is seen as well. The sharp extra band at 3705 cm^{-1}

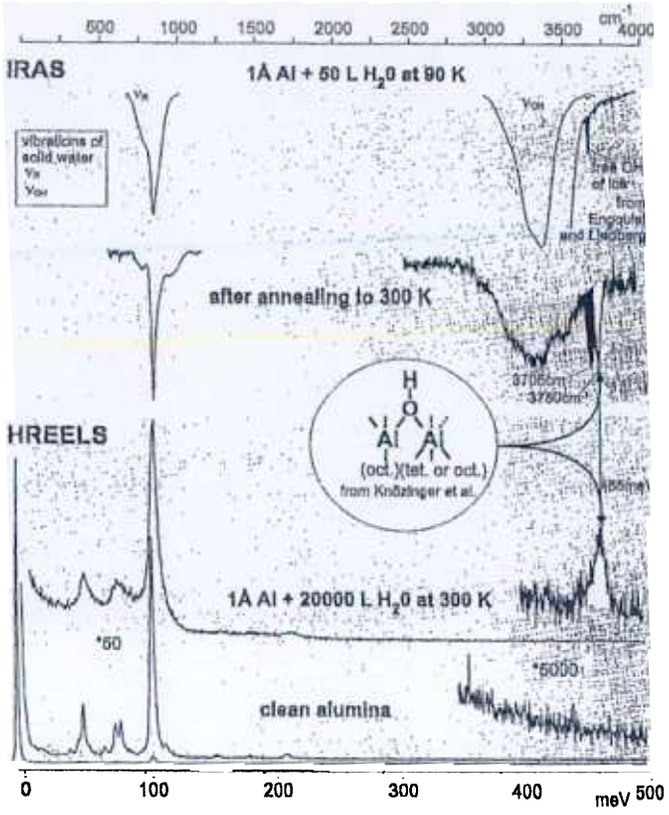

FIG. 10. Fourier transform IR spectra (RAIRS) and electron energy loss spectra (EELS) of a clean and OH (+H_2O)-covered alumina layer.

indicates free OH groups at the surfaces of these water clusters (*80*), as is also known from the surface of ice. Indeed, when a thick ice layer is grown on the alumina layer, this vibration is observed (Fig. 10).

By comparison with literature data (*81*), it is possible to assign the hydroxyl loss on the alumina surface. According to Knözinger (*78*), an OH vibration at 3750 cm^{-1} is characteristic of hydroxyl groups bridging aluminum ions, either both in octahedral sites or one in an octahedral and the other in a tetrahedral site. On alumina layers grown on a different NiAl substrate, other types of OH species may be formed. Therefore, it is conceivable that the influence of the nature of the hydroxyl species on the interaction with additional adsorbates (e.g., metal deposits) could be investigated.

Before we discuss metals on oxides, we describe the adsorption of CO_2 on oxides as an example of a molecular adsorbate system with more degrees

of freedom. Figure 11 shows TDS spectra of CO_2 from a clean, flashed Cr_2O_3(0001) surface (*26, 82*). The surface exhibits a structure discussed previously. The TDS spectra indicate that there are more weakly and less weakly bonded CO_2 species on the surfaces. We have investigated the nature of these species by various techniques including IR spectroscopy. Figure 11 shows several sets of IR spectra. The pair of sharp bands at approximately 2300 cm^{-1} is easily assigned to the more weakly bonded CO_2, which is only slightly distorted relative to the gas-phase species. A combination of isotopic labeling of the adsorbed CO_2 (leading to a shift of frequencies) and of the oxide layer (no shift of CO_2 islands) demonstrated that the single band centered at approximately 1400 cm^{-1} is indicative of the presence of a carboxylate species (i.e., a bent anionic CO_2 species) and not, as perhaps would have been expected, a carbonate (*83*).

The bands between 1610 and 1700 cm^{-1} are missing because of surface selection rules which apply to the thin-layer systems. This means that all non-totally symmetric bands are suppressed in intensity. A quick comparison with CO_2 adsorption on chromia microcrystalline material (Fig. 11) reveals the presence of the bands between 1610 and 1700 cm^{-1}, as expected for adsorption on a bulk dielectric material. The similarity between the

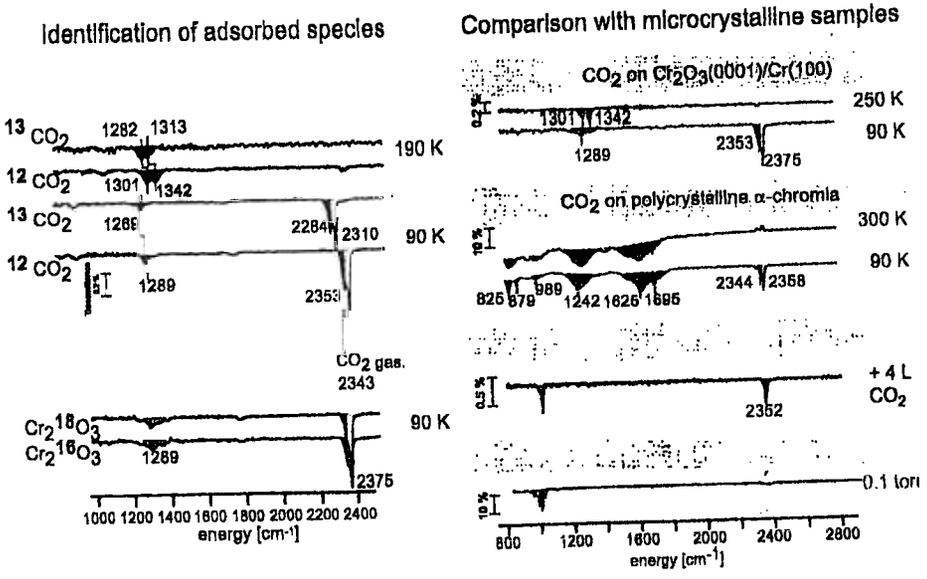

FIG. 11. RAIRS spectra of CO_2 adsorbed on Cr_2O_3(0001) and on polycrystalline chromia. (Left) RAIRS spectra at different surface temperatures with isotopically labeled CO_2 and Cr_2O_3. (Right) Adsorption of CO_2 after preadsorption of oxygen.

thin-layer data and the results for the microcrystalline material are remarkable, as discussed in detail by Seiferth *et al.* (*26*). Furthermore, the responses of the two systems to preadsorption of oxygen are comparable. As shown in Fig. 11, CO_2 adsorption in the form of the less weakly bonded CO_2^- is fully suppressed on the thin layer and very strongly attenuated on the microcrystalline sample. These results indicate that CO_2 occupies the chromium sites because we know that oxygen from the gas phase adsorbs on the chromium ions.

A comment concerning the electronic structure of the $Cr_2O_3(0001)$ surface is appropriate here. Electron loss (*84*) and X-ray photo electron (*85*) spectra have shown that the chromium ions in the surface are in a low oxidation state (i.e., Cr^{2+}), in contrast to chromium ions in the near surface and bulk regions. It is therefore not surprising that such a surface can provide electrons to adsorbed molecules, leading to an electron transfer as shown, for example, by the formation of O_2^- and CO_2^-. The low valence state of the chromium surface ions also has consequences in other reactions, such as the polymerization of ethene [this reaction has been carried out on $Cr_2O_3(0001)$ (*86*)], and in connection with other, more realistic model investigations (*87*).

An area that has not been investigated at all with regard to well-characterized single-crystal oxide surfaces is the photoinduced chemical reaction of large molecules. Photoinduced desorption of small molecules, CO and NO, from oxides, however, has been investigated extensively (*88–91*). Yates and Wovchko (*92*) reported such investigations of powder samples (i.e., rhodium complexes deposited on Al_2O_3 powder), including results characterizing C–H bond activation. We refer to the literature (*92*) for details and note that this should be considered as a new, promising area in connection with single-crystal systems.

III. Metals on Oxides

So far, we have considered clean oxide surfaces and their reactivities. In this section, we deal with the modification of the oxide surface resulting from deposition of metals. This represents a route toward the preparation and characterization of more complex model systems in heterogeneous catalysis that bridge the materials gap.

In the preceding few years, several strategies have been followed along this route (*1*). In early work, small metal particles were deposited onto oxide bulk single-crystal surfaces, particularly MgO, and characterized by transmission electron microscopy (TEM). Poppa (*14*) was the pioneer in this field; important contributions have been reviewed by Henry (*6*), who was involved in the early TEM measurements.

The early efforts were primarily aimed at the preparation of small, well-defined metal particles; another strategy has been followed by Møller *et al.* (*93–96*) and Diebold *et al.* (*12*), who prepared thin metal layers on bulk oxide single crystals such as $TiO_2(110)$. As mentioned previously, the advent of STM has had a substantial influence on the understanding of the structures of clean oxide surfaces. Several groups (*97–99*) have begun investigating metal deposition on TiO_2 surfaces. Interesting initial results have been obtained concerning metal particle migration and oxide migration onto the metal particles (the so-called SMSI effect) (*98, 99*). Particularly well-suited to the application of STM are metal particles deposited onto thin-layer oxide surfaces (*6, 7, 11, 13*). Goodman's group (*11*), for example, has made major contributions to this field. One of the early results of his group was obtained for copper aggregates deposited on an amorphous silica layer (*100*).

Recently, it has been shown that ordered thin silica layers can be grown (*101*). In our laboratory, a silica layer has been grown on Mo(112). Figure 12 shows a LEED pattern of the layer prepared by evaporation of silicon and subsequent oxidation. The surface has hexagonal symmetry, but its

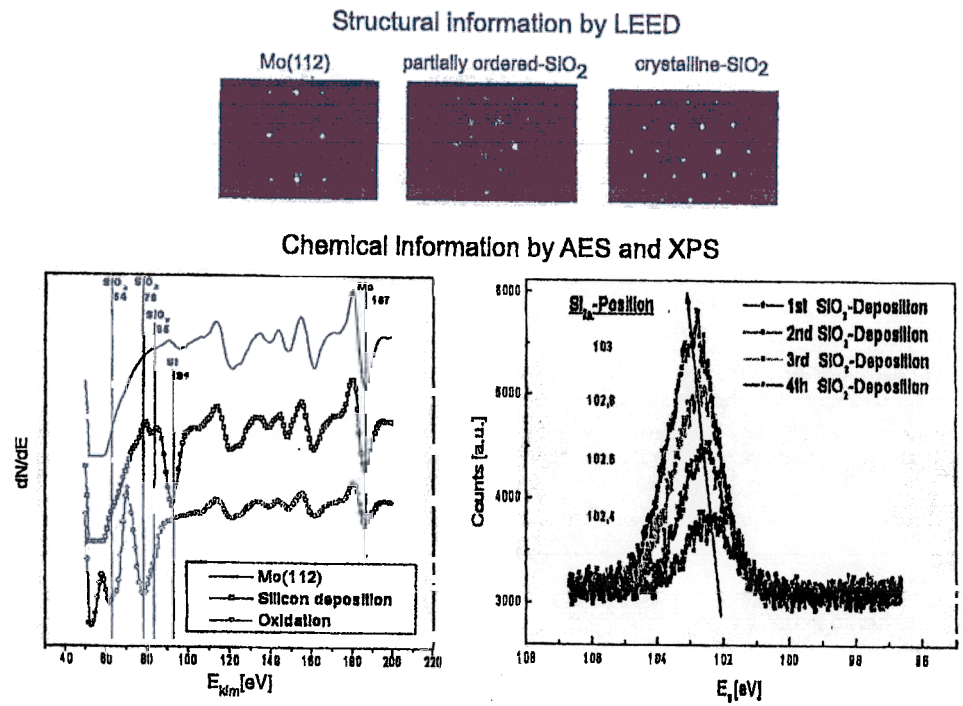

FIG. 12. LEED pattern and Si 2p spectra of a SiO_2 layer grown on Mo(112).

detailed structure is not known. Included in Fig. 12 is a set of Si_{2p} photoelectron spectra shown as a function of layer thickness and preparation conditions. The value observed for the final preparation is practically identical to that observed for thin silica layers on silicon, which are generally known to be amorphous (*102*). These layers will be used in the future as supports for evaporated metal aggregates.

In the past, we primarily used well-ordered alumina layers as substrates; Fig. 13 shows the result of an STM investigation. The left panel shows the clean alumina surface as imaged by a scanning tunneling microscope (*103*). The surface is well ordered, and there are several kinds of surface defects. One constitutes reflection domain boundaries between the two growth directions of $Al_2O_3(0001)$ on the NiAl(110) surface, the substrate on which the layer was grown according to a well-established oxidation recipe (*79*). There are anti-phase domain boundaries within the reflection domains and, in addition, point defects which are not resolved in the images. The image does not change dramatically after hydroxylation of the layer, a procedure which was mentioned previously (*76*). The additional panels show STM images of rhodium deposits on the clean surface at low temperature and at room temperature (*10, 104*) as well as an image recorded after deposition of rhodium at room temperature on a hydroxylated substrate (*105*). The amount deposited onto the hydroxylated surface is equivalent to the amount

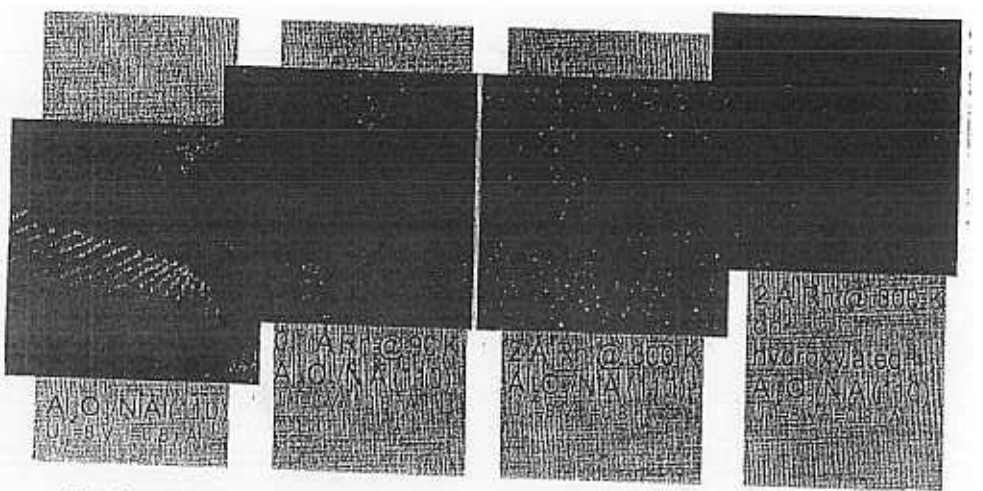

FIG. 13. Scanning tunneling microscopic images of a clean alumina layer (from left to right) after deposition of 0.1 Å of rhodium at 90 K, after deposition of 2 Å of rhodium at 300 K, and after deposition of 2 Å of rhodium at 300 K onto the prehydroxylated alumina layer. All scans: 3000 × 3000 Å.

deposited onto the clean alumina surface at room temperature. Upon vapor deposition of rhodium at low temperature, small particles are observed to nucleate on the point defects of the substrate, giving a narrow distribution of particle sizes. When the deposition of rhodium is carried out at room temperature, the mobility of rhodium atoms is considerably higher than at low temperature so that nucleation at the line defects of the substrate becomes dominant. Consequently, most of the material nucleates on reflection domain and anti-phase domain boundaries. The particles are relatively uniform in size, with the size depending on the amount of material deposited. When the same amount of material is deposited onto a hydroxylated surface, the particles are considerably smaller and distributed across the entire surface, i.e., a much higher metal dispersion is obtained (*76*).

The thermal behavior of the deposits is important to chemical reactivity because the particles may undergo morphological changes to adopt their equilibrium shapes, which could depend on whether or not a reactive gas phase is present. In the present case, detailed experiments have been undertaken to characterize the particles deposited onto the clean substrate, and less detailed experiments have been done to characterize the deposits on the hydroxylated surface (*10*). As a result of these investigations, it is known that the morphology of the ensemble is not altered within a temperature window from 90 to approximately 450–600 K. The window is extended to even higher temperatures when the substrate is hydroxylated. At temperatures above the upper limit, the particles tend to sinter, and they also start to diffuse through the layer into the metal substrate below (*10*).

This sintering process is an interesting subject in its own right, and research on this process is just beginning (*10*). A more basic issue, of course, is the metal atom diffusion on oxide substrates. The obvious technique to use in such an investigation is STM (*106*). However, in contrast to investigations of diffusion on metal surfaces, similar investigations of diffusion on oxide surfaces have not been reported. On the other hand, field ion microscopy characterizations of metal atom diffusion on oxide layers have begun, and a first estimate of activation energies for diffusion has been reported (*107*).

It is obvious that diffusion studies will profit from atomic resolution imaging, once it is obtained routinely for deposited aggregates on oxide surfaces. Whereas for TiO_2 and a few other oxide substrates atomic resolution may be obtained routinely, there are only a few reported investigations of deposited metal particles at atomic resolution (*108*). The first report of an atomically resolved image of a palladium metal cluster on MoS_2 was reported by Piednoir *et al.* (*108*). Atomically resolved images of palladium aggregates deposited on a thin alumina layer have also been obtained (*109*). Figure 14 shows an image of an aggregate of approximately 80 Å in width.

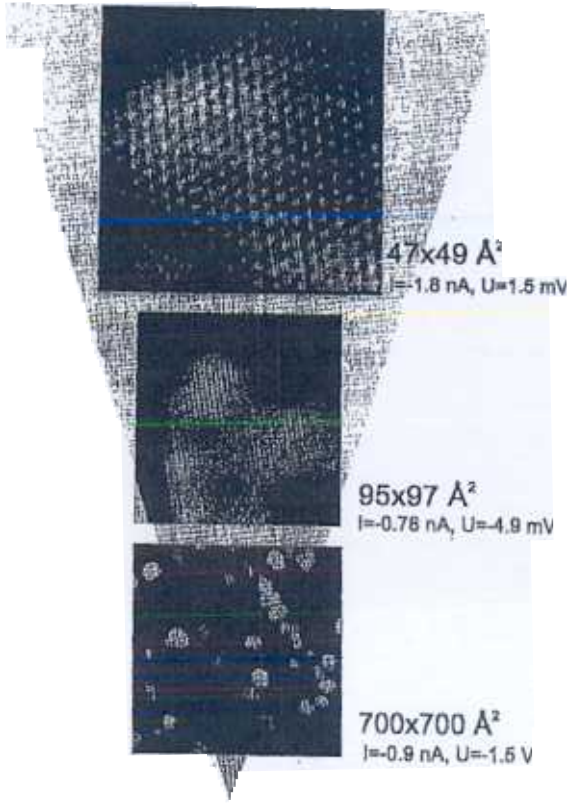

FIG. 14. Atomically resolved scanning tunneling microscopic images of palladium aggregates grown on an alumina layer [reproduced with permission from Hansen *et al.* (*109*)].

The particle is obviously crystalline and exposes on its top a (111) facet. Furthermore, on the side, (111) facets (typical of a cuboctahedral particle) can be discerned. The small (100) facets predicted for the equilibrium shape on the basis of the Wulff construction could not be atomically resolved.

However, if we apply the concept of the Wulff construction, we may deduce the metal surface adhesion energy (*109*). The basic equation is

$$W_{adh} = \gamma_{oxide} + \gamma_{metal} - \gamma_{interface} \quad (1)$$

Provided the surface energies (γ_{metal}) of the various crystallographic planes of the metal are known (*110*), a relative work of adhesion (W_{adh}) may be defined (*109*). We find a value of 2.9 ± 0.2 J/m² eV, which is still different from the result of recent calculations by Bogicevic and Jennison (*111*), who

reported metal adsorption energies of 1.05 J/m² calculated for a thin defect-free alumina layer. It is not unlikely that this discrepancy is related to the complicated nucleation and growth behavior of the aggregates involving defects of the substrate.

Although STM reveals the surface structure of deposited particles, their internal structure, in particular as a function of size, is not easily accessible from STM images. In this regard, TEM images of the same model systems can be of help (*112*). Figure 15 shows a schematic drawing of a sample. After growth of the layer and deposition of the particles, the sample is ion milled from the back so that a small hole is finally formed. In this way, a wedge is obtained which is thin enough for the imaging process.

An added benefit of this procedure is that the unsupported layer next to the edge can also be investigated (*113*). This capability provides the opportunity to assess whether the metal substrate has any structural effect on the deposits. On the basis of numerous high-resolution TEM (HRTEM) images and a subsequent analysis of the Moiré periodicities, it has been possible to calculate the lattice constants as a function of particle size (*112*).

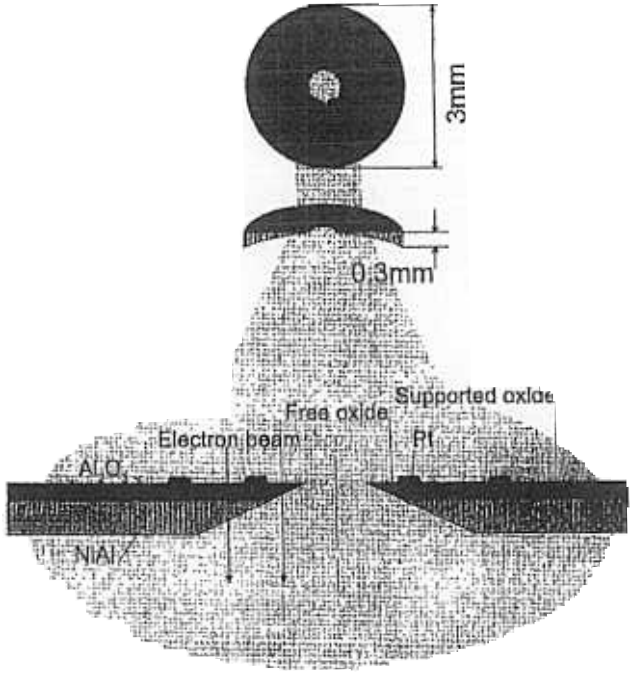

FIG. 15. Schematic drawing of a sample prepared for transmission electron microscopy

The corresponding plot is depicted in Fig. 16 and indeed demonstrates that the atomic distances decrease continuously to 90% of the bulk value at a cluster size of 10 Å. On the other hand, the lattice constant approaches the platinum bulk value even at a diameter of 30 Å. This effect has also been detected for tantalum and for palladium clusters on thin alumina layers, but it seems to be less pronounced in these cases (*114, 115*).

The deposits discussed so far were prepared with the intention of maintaining the size distribution narrow. The spacing of aggregates on the surface, however, has not been an issue. If we consider reacting systems, diffusion of species between the particles (i.e., spillover processes) may become important. Therefore, it may be desirable to control not only the particle size and morphology but also the distances between particles. Several methods have been used, but we refer only to those based on electron beam lithography. Rupprechter *et al.* (*116, 117*) reported the preparation of two-dimensional arrays of platinum particles deposited onto amorphous SiO_2 layers. Particles of 25- to 40-nm average size were produced, as shown in Fig. 17. The atomic force microscopy (AFM) image reveals an average height of 20 nm for these particles, which were obtained after several reaction-cleaning cycles. Other, similar images have been reported (*118–122*). The average metal particle size reported in these investigations is still an order of magnitude larger than that of the particles nucleated and grown under UHV conditions.

There are other methods to prepare model systems which are not classified according to Fig. 1. One is the preparation of "inverse" model systems consisting of oxide islands grown on metallic supports. The idea is to leave parts of the metal support uncovered so that the interface between meal and oxide is exposed. Several groups (*123–126*) followed such routes. We refer to the literature for details and restrict this discussion to the deposited metal aggregates on oxides.

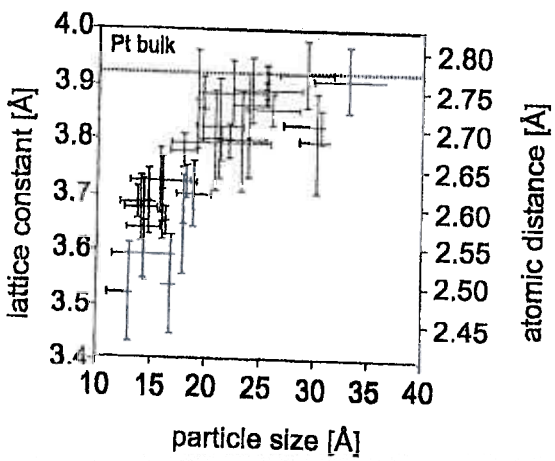

FIG. 16. Lattice constants and interatomic distance of platinum particles grown on Al_2O_3/NiAl(110) as a function of their size. (The ends of the horizontal bars represent the width and the length of the particular particles, respectively, and the vertical bars are error bars.)

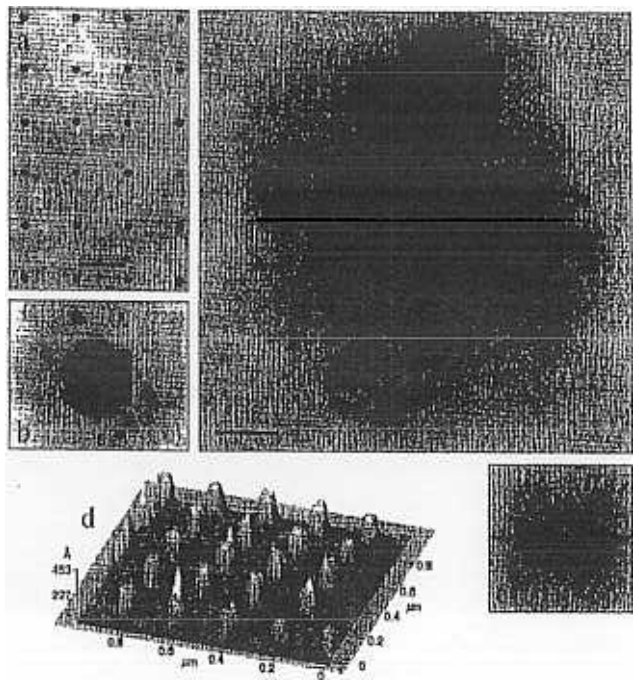

FIG. 17. (a) Transmission electron micrograph of a platinum nanoparticle array on SiO_2 (mean particle diameter, 40 nm; interparticle distance, 230 nm). (b) Microdiffraction pattern of an individual platinum particle showing its polycrystallinity [spots originating from a (110)-oriented crystalline grain within the polycrystalline platinum particle are marked by circles]. (c) HRTEM micrograph and (c') fast Fourier transform of a 25-nm platinum model catalyst particle. (d) AFM image of a platinum nanocluster array after several reaction-cleaning cycles.

Of course, the electronic structure of deposited metal aggregates reflects the geometric structure to a degree and vice versa. The electronic structure, which is discussed next, has been investigated using various methods, including photoemission, X-ray absorption, and scanning tunneling spectroscopy. One particularly interesting aspect is the size dependence of the electronic structure in relation to adsorption and reactivity.

Starting from an atomic-level diagram, Fig. 18 shows the development when increasingly more atoms are agglomerated to form an aggregate and finally a solid with a periodic lattice. Upon formation of an aggregate from equivalent atoms, the atomic levels are split into molecular orbitals, many of which are degenerate if the symmetry of the system is high. The splittings are characteristic of the interatomic interactions. Depending on the interaction strength, the split levels derived from a given atomic orbital start to overlap energetically with levels derived from other atomic orbitals. As long as the system has molecular character, there is an energy gap left between occupied and unoccupied levels. This situation is in contrast to that encountered for an infinite periodic metallic solid, as presented on the right-hand side of Fig. 18: where there is no longer a gap between occupied and unoccupied levels. It is not difficult to envision that, as the number of atoms in an agglomerate is slowly increased, the gap between occupied

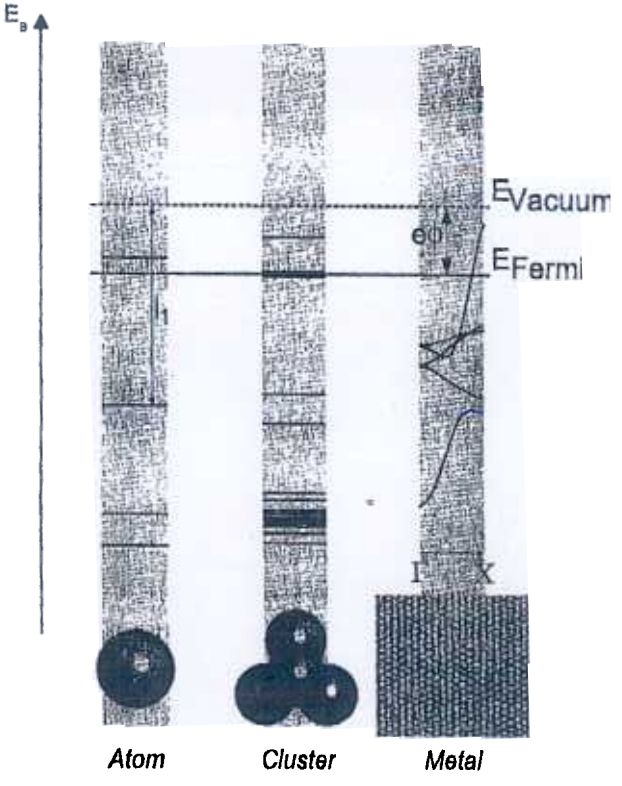

FIG. 18. Diagram illustrating the transition from an atom to a metal.

and unoccupied orbitals effectively vanishes. This is the case if the gap decreases to a value close to kT. In this situation, the changes in the electronic structure would be responsible for an insulator (molecule)–metal transition.

The question arises as to how many atoms are necessary to induce such a transition. There are several reports claiming numbers ranging from 20 to several hundred atoms in this respect (*115, 127–140*). An interesting extrapolation was deduced from spectroscopic measurements of the gap of inorganic carbonyl cluster compounds as a function of the cluster size. The result is shown in Fig. 19 (*129*). The extrapolation suggests that 70 atoms are sufficient to close the gap. The extrapolation yields a vanishing gap just below 100 metal atoms.

On the other hand, we have investigated deposited clusters of varying size with a combination of photoelectron spectroscopy (*132, 141*) and

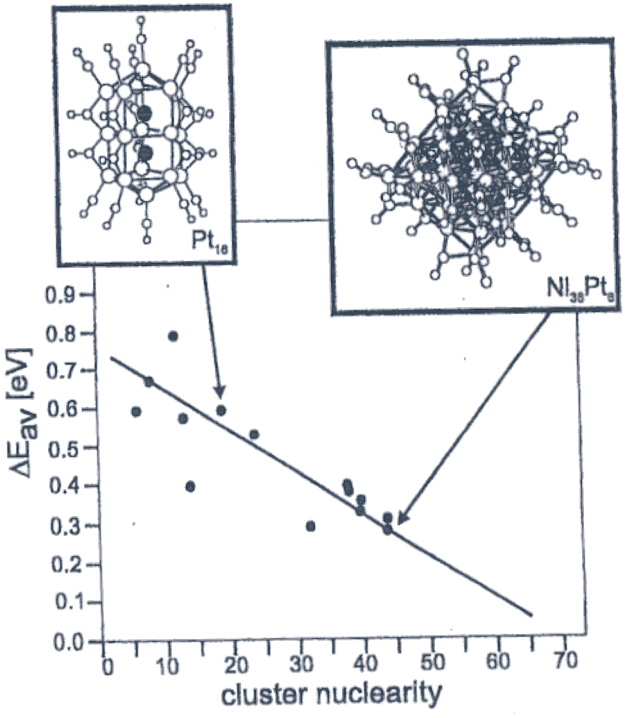

FIG. 19. Electronic excitation of lowest energy for several cluster compounds as a function of the number of metal atoms in the cluster [reproduced with permission from de Biani *et al.* (*129*)].

X-ray absorption (*140*). Figure 20 shows the chemical shifts measured for aggregates of palladium and of rhodium of varying size and plotted as a function of the inverse diameter (*130, 140, 142–148*). There is a linear correlation characterizing the clean as well as the CO-covered aggregates. It has generally been accepted (*130, 140, 142–148*) that this behavior is typical of the response of metallic spheres on the creation of a core hole, which in turn is screened by the metal electrons of the sphere. The different slopes for the clean and the CO-covered clusters can be explained by the electron-withdrawing effect of the adsorbed CO molecules. The withdrawal of charge from the clusters changes the effective electron density in the cluster and the screening properties. The plots are fully compatible with a metallic behavior, and there is no clear indication for a metal-to-non-metal transition.

According to the calculation characterizing gold clusters (*149*), this is not surprising. The screening properties are governed by the dielectric function. Its value is infinite for a metal, and it is still very large for a finite cluster, even though the cluster may have developed a small gap between occupied and unoccupied levels. This makes it hard to use the results as

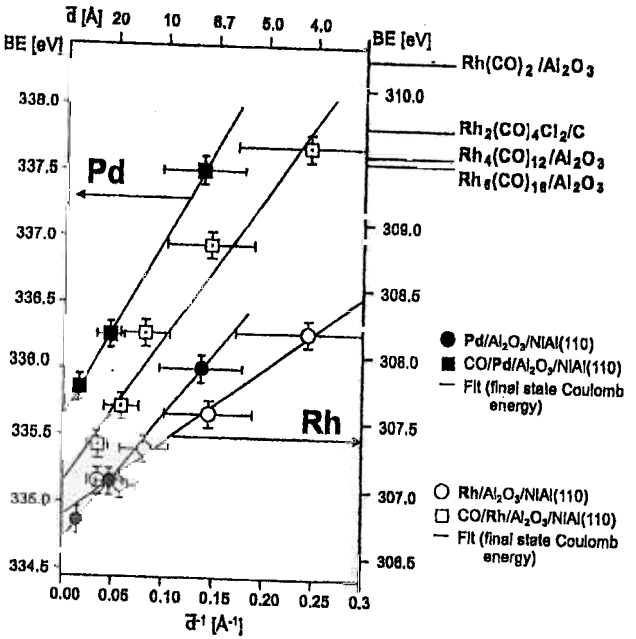

FIG. 20. Shift of XPS binding energies as a function of aggregate size for palladium aggregates and rhodium aggregates.

test cases. Therefore a second set of experiments (*140*) has been undertaken for CO-covered palladium clusters exclusively (Fig. 21).

The C 1s ionization potentials of CO molecules adsorbed on palladium aggregates of different size have been measured. The ionization potential is then compared with the onset of X-ray absorption of light in the wavelength region where the C 1s–2π absorption is observed. The lowest wavelength where this adsorption can be induced corresponds to a state of the system in which screening is optimal and the system can attain the state of lowest energy. In a photoelectron spectrum, on the other hand, where a C 1s core hole is created and charge is transferred from the metal particle to the 2π unoccupied states to screen the core hole, the same screened state of the system is obtained. In other words, the C 1s ionization potential is pinned to the onset of the X-ray absorption Pd 4d–CO 2π band (*150, 151*).

Again, this is the situation if the aggregate is a metal. However, if the aggregate is not metallic, then this relationship does not hold, and thus the ionization potential floats with respect to the onset of the X-ray absorption spectrum. Consequently, in the case of a nonmetal-to-metal transition, we

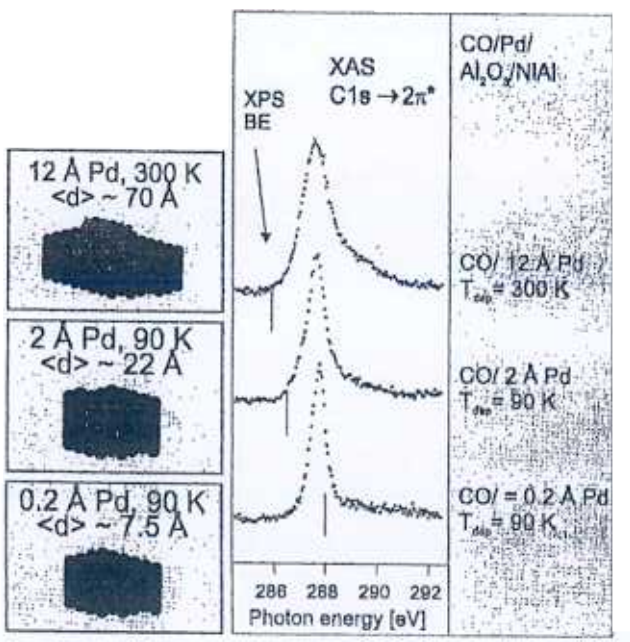

FIG. 21. X-ray absorption spectra of CO adsorbed on palladium aggregates of varying size. The ionization potentials as derived from photoelectron spectra are marked in the spectra.

observe a switch from a situation with floating Fermi levels to a pinning of the X-ray onset to the ionization potential.

Figure 21 shows a set of X-ray adsorption spectra and also the positions of the corresponding ionization potentials for various cluster sizes. Whereas for the larger cluster sizes there is a clear pinning of the Fermi energy indicating a metallic state of the system, the onset of the X-ray absorption spectrum does not align with the ionization energy for the small cluster sizes. It appears that such a situation is reached when the diameter of the aggregate decreases to values below 25 Å diameter and a height of 15–20 Å. The aggregate of this size contains 75–100 atoms, and the size correlates with the extrapolation of the spectroscopic data of metal carbonyl cluster compounds discussed in connection with Fig. 19 as well as with our results. We consider this comparison as a strong indication that, at least for the carbon monoxide-covered clusters, a nonmetal-to-metal transition occurs in the vicinity of such a size.

Goodman and his group used scanning tunneling spectroscopy to investigate the electronic structure of aggregates deposited on oxides (*152*). Figure 22 shows typical current–voltage curves for some aggregate sizes, i.e., gold on $TiO_2(110)$ (*77*). Although the large particles do not exhibit a plateau near $I = V = 0$, the smaller clusters do show the behavior expected for a system with a gap. However, the discrete structures observed for other systems (i.e., nanoparticles on graphite and related substrates) are not found (*109, 153, 154*). The authors (*77*) report indications that it is particularly the second layer in the gold aggregates that is responsible for the nonmetal-

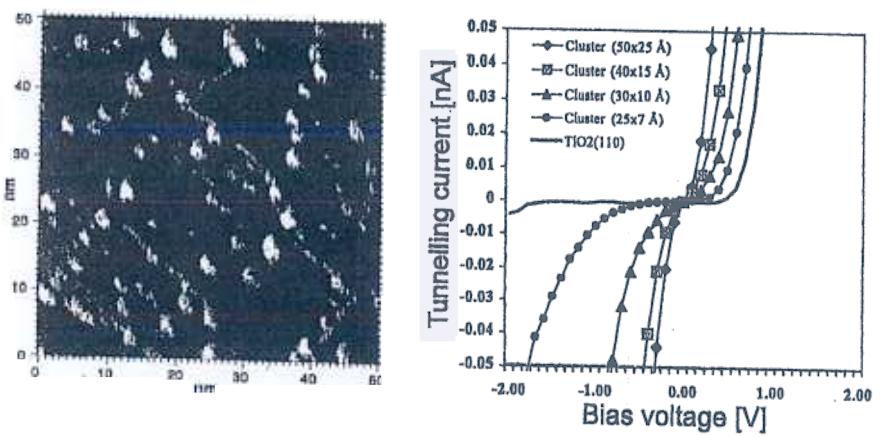

FIG. 22. Current–voltage curves determined for clusters of various sizes in the Au/$TiO_2(110)$ system as depicted in the STM image [reproduced with permission from Valden and Goodman (*77*)].

to-metal transition. Gold is an interesting low-temperature CO oxidation catalyst and we return to this when we discuss chemical reactivities.

Another particular aspect of the electronic structure is the magnetic behavior of small particles (*155*). Although much is known about thin metal layers in UHV as well as about supported powder catalysts, studies of magnetic properties of deposited particles under well-defined conditions are very rare (*156–159*). We briefly mention here studies using the technique of ferromagnetic resonance spectroscopy (Fig. 23), a modification of electron spin resonance.

Aggregates of iron and cobalt have been studied after deposition onto

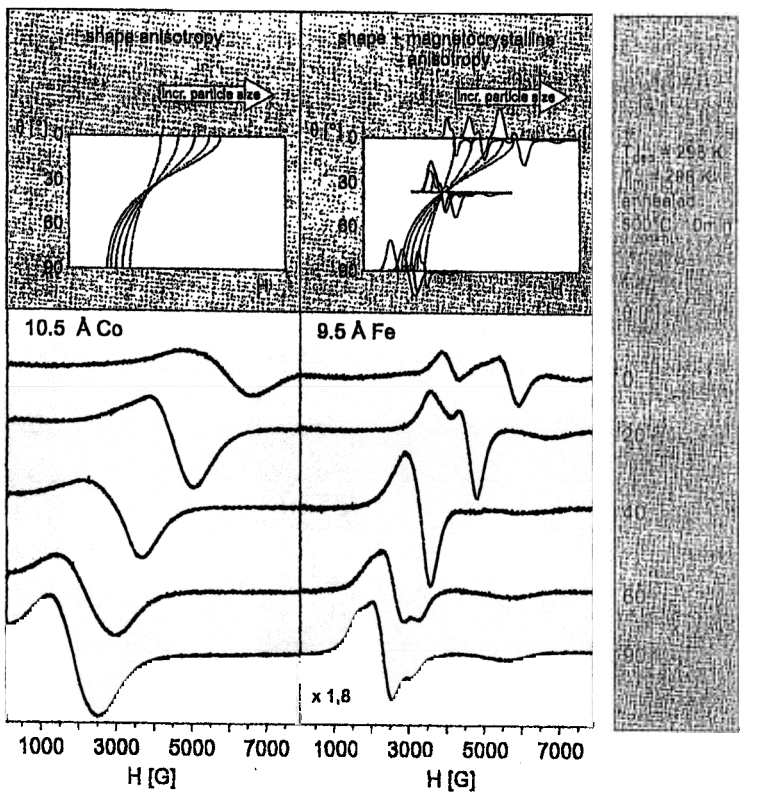

FIG. 23. Ferromagnetic resonance spectra taken for cobalt aggregates deposited on sapphire (left) and iron aggregates on sapphire (right). The angle of the magnetic field was varied with respect to the surface normal. The insets show the theoretically expected angular dependencies as a function of the deposited amount (left) for a layer with particles exhibiting uniaxial anisotropies (right, with particles with triaxial anisotropies).

alumina, prepared both as a thin layer and as bulk alumina, i.e., sapphire substrate. The dispersion of the particles has been investigated by STM and their magnetism by angle-dependent ferromagnetic resonance (FMR) measurements of the kind shown in Fig. 23 for two particle size distributions. The particular data have been taken for iron particles of 30–40 Å. The observed line shape and resonance frequency changes as a function of the angle of the external magnetic field can be fit by assuming a particle size distribution of the log normal type and a dependence of the magnetic properties of the particles as a function of their size. A schematic diagram taking the various contributions into account is included in Fig. 23. The resonance position of the absorption changes as the angles between external field and surface normal are varied. The magnetic anisotropy is the reason for this behavior. For the different particle sizes, characteristic variations in the anisotropy are expected ranging from a strong dependence for the large particles to a weak dependence for the small particles. The weak dependence is characteristic of superparamagnetic particles. For each size, a line shape has to be chosen. The superposition then results in the variations observed in Fig. 23. The presented data and the analysis are only preliminary and more detailed measurements and simulations have to be performed.

It is yet to be determined to what degree these magnetic properties can be used in applications, such as sensors and information storage. The FMR signal can be used, of course, to monitor the magnetic properties of the particles even under ambient conditions, when X-ray photoelectron spectroscopy (XPS) and other surface-sensitive tools fail, because the measurement relies on photons.

Before further discussing the reactivities of deposited particles, we briefly discuss adsorption properties using CO as a probe molecule. An advantageous technique to study CO adsorption is FTIR spectroscopy because it provides the resolution to differentiate between various adsorbed species. Again, the thin-layer-based systems are particularly well suited since the metallic support of the oxide layers acts as a mirror at IR frequencies. However, it is also possible to perform such experiments on surfaces of bulk dielectrics as shown by the Hayden group (*160, 161*).

Rainer and Goodman (*152*) published a study of CO adsorption on palladium aggregates on Al_2O_3 layers. The results have been interpreted as characteristic of the adsorption of CO on different facets of the small crystalline aggregates. Although this interpretation does not take into account adsorption on the various defect sites of the aggregates (*132*), as pointed out recently (*162*) the data are indicative of the potential of this technique for the characterization of size-dependent absorption phenomena.

We recently prepared metal deposits on well-ordered alumina layers at

low temperatures in the range of 50 to 90 K (*163, 164*) to determine the IR characteristics of specific sites. The IR spectrum characterizing a rhodium deposit prepared and saturated with CO at 90 K (the average cluster contained nine atoms) is displayed in Fig. 24a (top). The most prominent feature in the stretching region of terminally bonded CO molecules is a sharp, intense band at 2117 cm^{-1}. This signal has previously been shown to arise from isolated rhodium atoms trapped at oxide defects (*162*). Both the number of adsorbed CO molecules and the nature of the defect site remained unclear. Features at lower frequencies, on the other hand, have been assigned to molecules on rhodium aggregates.

To gain insight into the stoichiometry of the rhodium carbonyl species giving rise to the band at 2117 cm^{-1}, isotopic mixture experiments were performed. If such a signal were indicative of Rh–CO, an equimolar mixture of ^{12}CO and ^{13}CO should result in the appearance of a second IR band of equal intensity about 47 cm^{-1} lower. In the case of $Rh(CO)_2$, three species of different isotopic composition would be formed with relative abundances 1:2:1, giving rise to three IR bands with intensities reflecting this ratio.

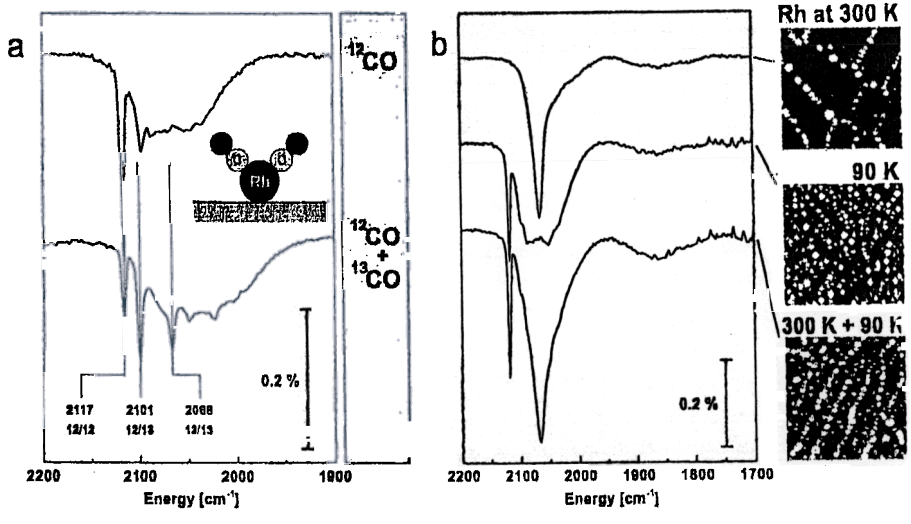

FIG. 24. (a) IR spectra taken after deposition of 0.028 monolayer (ML) of rhodium and subsequent saturation with ^{12}CO (top) and an approximately equimolar mixture of ^{12}CO and ^{13}CO (bottom) at 90 K. The isotopic compositions giving rise to the three dicarbonyl bands are indicated below the corresponding wavenumbers. The average particle contained nine atoms. (b) IR spectra recorded after CO saturation of rhodium deposits at 90 K, along with corresponding room-temperature STM images (500 × 500 Å). Top, 0.057 ML of rhodium deposited at 300 K; middle, 0.057 ML of rhodium deposited at 90 K; bottom, 0.057 ML of rhodium deposited at 300 K, followed by the same exposure at 90 K.

The latter observation was indeed made experimentally (Fig. 24a, bottom), thereby showing that $Rh(CO)_2$ is responsible for the IR band under investigation. Such rhodium gem-dicarbonyl species, with a rhodium oxidation state of 1, result from the disruption of metal crystallites on Rh/Al_2O_3 catalysts (symmetric stretch, ~2100 cm^{-1}; antisymmetric stretch, ~2035 cm^{-1}) (*165–167*). These bands have also been observed by the group of Solymosi, who characterized rhodium on $TiO_2(110)$ single crystals (~2110 cm^{-1}/~2030 cm^{-1}) (*160, 161*), and followed a similar disruption process by STM (*168*).

No signal is discerned in our data that is indicative of the antisymmetric stretch (Fig. 24a). Since for thin oxide layers on metal substrates the surface selection rule applies, its dynamic dipole moment must be oriented parallel to the oxide surface.

We now discuss the type of rhodium nucleation site responsible for the IR band at 2117 cm^{-1}. Rhodium deposition at room temperature results in the formation of metal aggregates located at oxide domain boundaries. Upon CO saturation at 90 K, no $Rh(CO)_2$ is formed (Fig. 24b, top). This is in clear contrast to what is observed for a low-temperature deposit. Nucleation inside the domains gives rise to the dicarbonyl band (Fig. 24b, middle). STM measurements showed that point defects are the primary nucleation sites under these conditions (*169*). Rhodium decoration of the line defects at room temperature preceding deposition at 90 K does not suppress rhodium dicarbonyl formation (Fig. 24b, bottom). Consequently, we may conclude that the $Rh(CO)_2$ species are not associated with the domain boundaries but rather with oxide point defects, which are the dominant rhodium nucleation sites at 90 K.

To reduce the particle sizes further, growth and adsorption experiments were performed at 60 K. In the IR spectrum of ^{12}CO adsorbed on such a rhodium deposit (the average cluster at 300 K incorporated five atoms), many distinct signals are observed at frequencies between 2172 and 1961 cm^{-1}, along with a broad absorption band in the range of 2120 to 1950 cm^{-1} (Fig. 25, bottom) and a very weak feature due to multiply coordinated CO at 1856 cm^{-1}.

As in the case of the deposits formed at 90 K, the broad band and the sharp feature at 2116 cm^{-1} are attributed to terminally bonded CO on rhodium aggregates of various size and to $Rh(CO)_2$ species at oxide point defects, respectively. Physisorption on the Al_2O_3 (*170*) is reflected by the band at 2172 cm^{-1}, which is also observed upon exposure of the pristine oxide layer to CO.

One or more new types of rhodium nucleation sites clearly come into play at 60 K, in contrast to the situation at 90 K, as indicated by the observation of a smaller mean particle size, by the lower intensity of the IR band due to rhodium nucleated at the point defects, and by the appearance of new signals at 2087, 2037, 1999, and 1961 cm^{-1}. The small half-

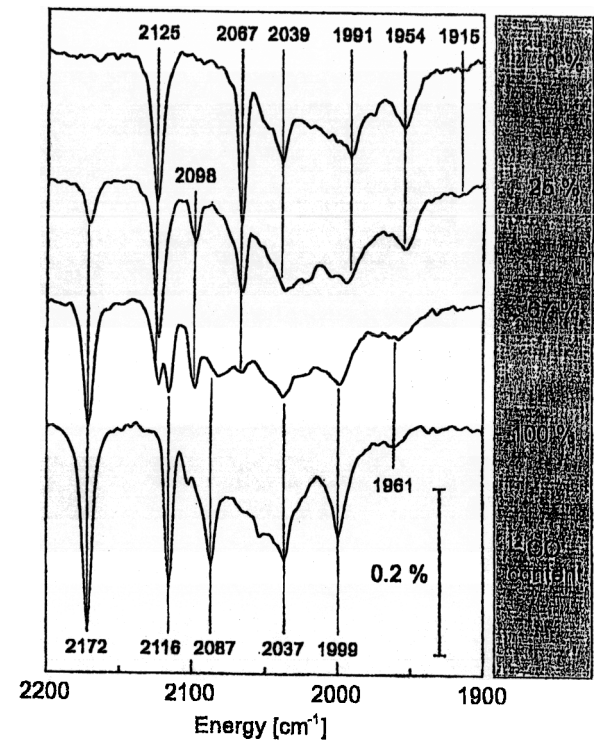

FIG. 25. Series of IR spectra acquired at 60 K after deposition of 0.020 ML of rhodium at 60 K and subsequent saturation with isotopic mixtures of ^{12}CO and ^{13}CO at the same temperature. The percentage of ^{12}CO is given next to the spectra. The average particle contained five atoms.

widths of the bands point to the presence of uniform, isolated $Rh_n(CO)_m$ species. Similar features are obtained for deposits with even lower mean particle sizes. Therefore, it is suggested that they most likely originate from atomic, dimeric, or possibly trimeric Rh–CO species.

Again, the use of isotopic mixtures provides additional information regarding the identities of the surface species. As expected, saturation with ^{13}CO results in a downward shift of the entire spectrum by 42–49 cm^{-1} (Fig. 25, top). Slight changes in relative band intensities are due to small variations in sample temperature. Following the spectral evolution with isotopic composition, differences in behavior of the individual bands are observed (Fig. 25):

1. As expected for single, isolated CO molecules, the intensities of the bands at 2172 and 2125 cm^{-1} vary linearly with the concentration of the corresponding isotopes.

2. In line with the statistics of mixtures, the rhodium dicarbonyl bands at 2116 and 2067 cm^{-1} are more strongly attenuated upon addition of the other isotope, and a band due to the mixed dicarbonyl is observed at 2098 cm^{-1}.

3. Between the bands at 1999 and 1954 cm^{-1}, no such signal at an intermediate frequency is found, implying that they do not originate from rhodium dicarbonyl species at a different surface site. Their slow intensity variation may indicate Rh–CO.

4. In clear contrast to this, the 2087-cm^{-1} band vanishes completely upon admixture of 33% ^{13}CO. This change is conceivable only if the surface complex contains three or more CO molecules.

The information gained from the other signals is less specific. In summary, we conclude that several different types of rhodium particles are responsible for the observed IR features. Currently, density functional calculations characterizing small rhodium carbonyls are in progress (*171*). Calculated vibrational frequencies of such systems may help to identify the species present on the alumina layer.

Studies characterizing small rhodium particles have been extended to neighboring elements in the periodic table. IR spectra recorded after deposition of comparable amounts of palladium, rhodium, and iridium and subsequent CO saturation at 90 K are displayed in Fig. 26. We note differences in the low-wavenumber region, where vibrational frequencies of molecules in multiple coordinated sites are found. As on single crystals, the population of such sites is highest on palladium (*172, 173*), whereas no such CO is observed on iridium (*174, 175*).

The differences in the region of terminally bonded CO, however, are much more pronounced. In the case of iridium, several distinct features are observed. In analogy to the $Rh(CO)_2$ band at 2117 cm^{-1}, the sharp signal at 2107 cm^{-1} may be attributed to $Ir(CO)_2$ species via isotopic mixture experiments (not shown). Bands with similar frequencies have been assigned to the symmetric stretch of $Ir^+(CO)_2$ on Ir/Al_2O_3 catalysts (2107–2090 cm^{-1}) (*176*) and on the iridium-loaded zeolite HZSM-5 (2104 cm^{-1}) (*177*). The appearance of many bands at lower wavenumbers is reminiscent of the rhodium deposits formed at 60 K (Fig. 26), indicating a comparable nucleation behavior.

In contrast to these results, no signs of atomically dispersed palladium or structurally well-defined aggregates are observed. Indeed, the IR spectrum is similar to that observed for much larger, disordered palladium aggregates (*162*). At the same metal exposure, the palladium particles are found to be larger than the rhodium aggregates by room-temperature STM.

Our observations show that IR spectra of adsorbed CO provide valuable

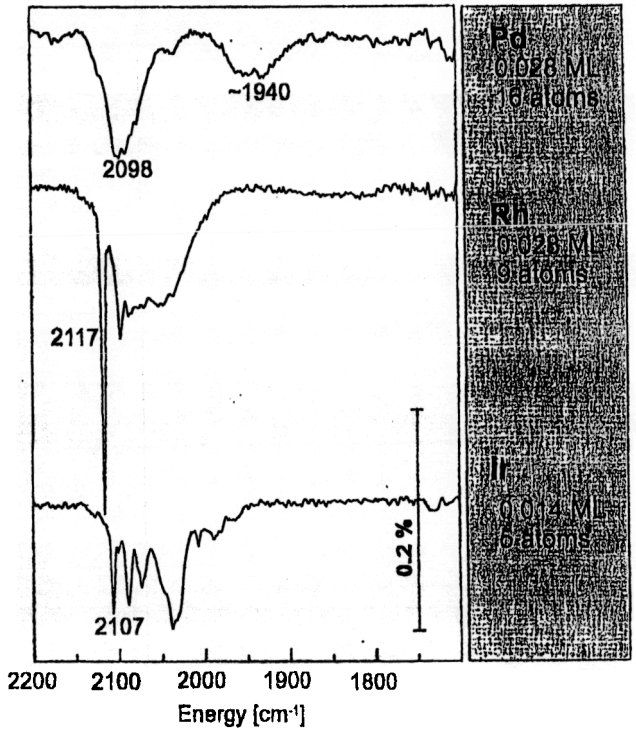

FIG. 26. IR spectra of palladium, iridium, and rhodium deposited at 90 K and saturated with CO at the same temperature.

information on the size of metal nanoparticles, as has long been recognized in the catalysis-related literature. The literature contains several adsorption studies (*178*) employing other probe molecules such as hydrocarbons, but in this case reaction also comes into play and renders the situation even more complicated.

Next, several simple chemical reactions of O_2, CO, and hydrocarbons on small aggregates are addressed. A simple reaction is the dissociative adsorption of oxygen on small particles. The palladium aggregate shown in Fig. 14 can be imaged at atomic resolution after a dosage to saturation with molecular oxygen from the gas phase (*179*). On the side facets the corrugation due to the presence of adsorption of oxygen can be identified. A doubled periodicity corresponding to a $p(2 \times 2)$ structure can be identified. This structure is very similar to the $p(2 \times 2)$ structure observed after dissociative oxygen adsorption on Pd(111) (*180*). We therefore conclude that a similar situation is encountered in the case of the deposited aggre-

gates. The p(2 × 2) structure interestingly appears on the different facets at different tunneling conditions. When the oxygen-covered palladium aggregates are exposed to carbon monoxide, the reactivity of the different facets appears to be different in the sense that the oxygen adsorbate structure is lost on the various facets at various temperatures and exposures. It will be interesting to investigate these effects in more detail.

CO oxidation has been characterized for gold aggregates supported on TiO_2 at low temperatures and as a function of particle size (*77*). Gold clusters ranging in diameter from 10 to 60 Å were prepared on titania single-crystal surfaces and exposed to O_2 and CO. It was deduced that the structure sensitivity of this reaction in this system is related to a quantum size effect with respect to the thickness of the gold islands on the TiO_2(110)-(1 × 1) surface. The result of these reaction experiments is shown in Fig. 27 (top). The authors found a marked size effect of the catalytic activity, which correlates with the original observations (*181*) for gold on high-area, titania-supported catalysts. The aggregates near 35 Å in diameter show the maximum activity.

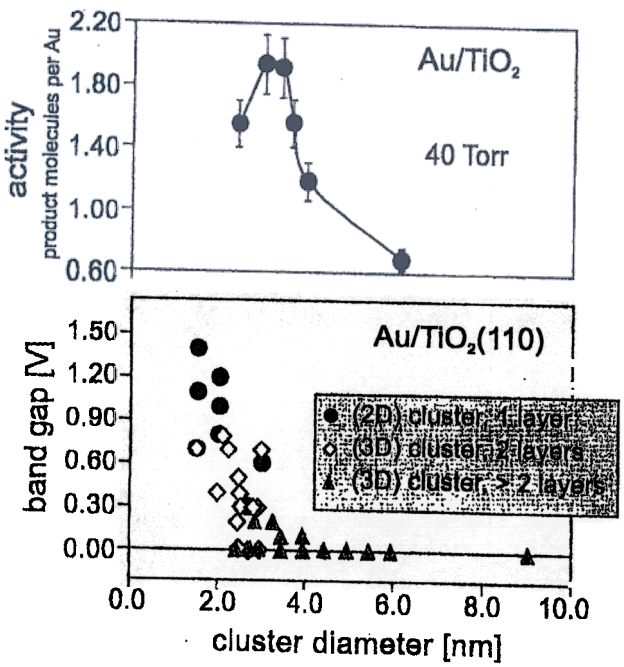

FIG. 27. Reactivity of size-selected gold aggregates deposited on TiO_2(110) (top) correlated with the band gap of the aggregate as deduced from STM current–voltage curves (bottom) [reproduced with permission from Valden and Goodman (*77*)].

In the future, it will be important to perform kinetics measurements for such reactions under well-defined conditions, in both UHV and ambient environments. A good example was recently reported (*182*)—a molecular-beam investigation of CO oxidation on palladium aggregates deposited on a MgO single crystal. The results shed light on how the rates are affected by the role of adsorbate diffusion on the MgO substrate, spillover to the metal deposits, and the role of different CO and O adsorption sites on the various facets of the aggregates. Kasemo *et al.* (*183, 184*) reported model calculations which consider the dependence of the kinetic phase diagrams (reaction rate versus reactant pressure) on the details of diffusion and sticking parameters on the crystallite facets. The experimental results from Henry's group (*182*) are compatible with such considerations.

In the work reported up to now, the aggregate distributions have not been monodisperse. However, Heiz *et al.* (*22, 185, 186*) reported adsorption and reaction experiments characterizing deposits of platinum and of gold aggregates on MgO layers; these were prepared from impinging size-selected, gas-phase clusters of the metal and inferred to be monodisperse, but they have not been imaged. The adsorbates were characterized by TDS

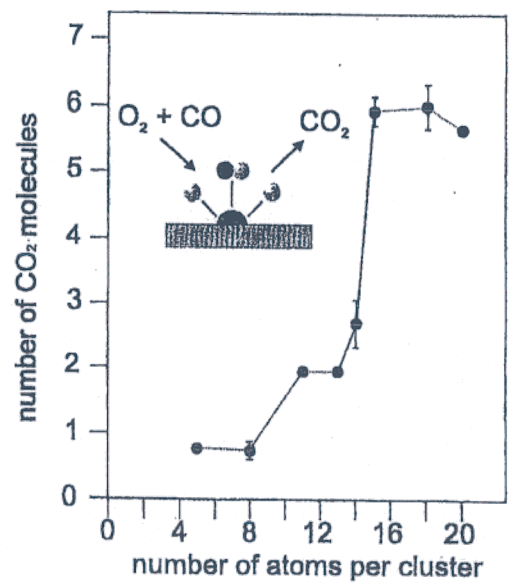

FIG. 28. Total number of catalytically produced CO_2 molecules as a function of cluster size. The clusters have been mass selected in the gas phase and deposited on a MgO film [reproduced with permission from Heiz *et al.* (*186*)].

and IR spectroscopy. The main reaction was CO oxidation; a typical result is shown in Fig. 28. It seems that with respect to the rate of the reaction, every atom of the aggregate counts in the regime of very small clusters.

Oxygen adsorption on palladium and on gold does not lead to oxide formation under the reported conditions, but it is expected that more reactive metals form oxides. We recently tested this assumption for tantalum aggregates and compared them with continuous tantalum layers (*187*). The continuous layer was oxidized to Ta_2O_5, as monitored with XPS, whereas the deposited aggregates adsorbed oxygen without being fully oxidized. On the other hand, cobalt and iron aggregates are easily oxidized under comparable conditions (*158*). This work needs to be extended to determine the effects of aggregate size.

Similar to experiments concerned with CO oxidation on gold aggregates summarized previously, we have undertaken an investigation of CO dissociation on rhodium particles (*188–190*). C 1s photoelectron spectra were recorded as a function of sample temperature and rhodium particle size. An example is shown in Fig. 29 for a temperature range in which the morphology of the ensemble of aggregates did not change. At low temperature, the signal typical of molecular CO was observed. At a temperature near 400 K a second signal appeared, indicating the dissociation of CO into carbon and oxygen atoms. At 500 K all molecular CO had been either dissociated or desorbed. The dissociation probability is then given by the ratio of the molecular to the atomic C 1s signal, which is plotted in Fig. 30 as a function of the aggregate size. Also included in Fig. 30 are data for very small aggregates, for which it has been shown that CO dissociation is negligible (*191*), as it is for close-packed, single-crystal surfaces (*192*), which correspond to the limiting case of infinitely large aggregate size. In contrast, the data obtained for stepped rhodium surfaces indicates that there is a probability for CO dissociation (*193*). The dissociation probability is highest for intermediate-sized aggregates consisting of 100–200 atoms.

Although electronic effects cannot be completely excluded as a reason for the onset of the dissociation phenomenon for small particles, an explanation on the basis of structural properties seems more likely. Since the rhodium deposits are basically disordered, it is easily imaginable that aggregates of medium size exhibit a maximum density of defects, such as steps, kinks, and other low-coordinated surface atoms. Smaller units are expected to contain fewer defects, especially if they are two-dimensional. Furthermore, spatial constraints may play a role [accommodation of carbon and oxygen atoms on adjacent sites (Fig. 30)]. At high exposures, the step density is reduced as a consequence of coalescence processes. For deposition at 300 K, the observed tendency to form crystalline aggregates in the high-coverage regime also contributes to a lower defect density, consistent with

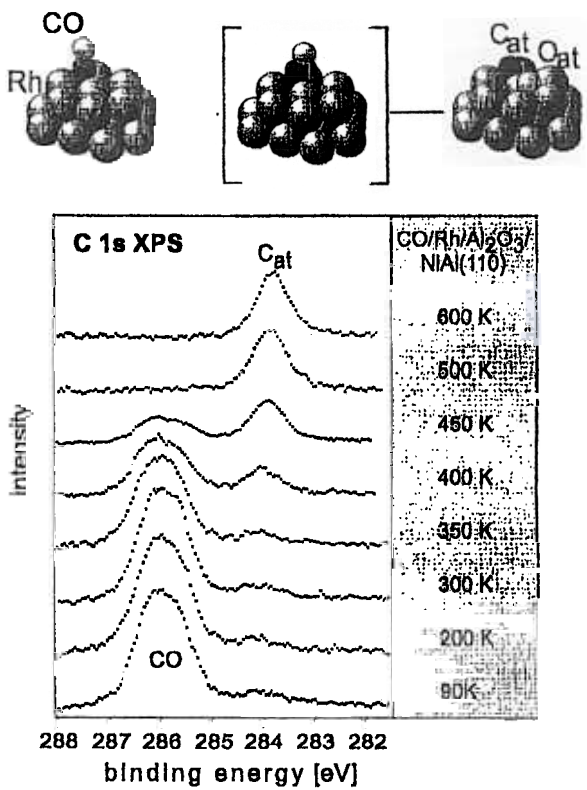

FIG. 29. CO dissociation on $Rh/Al_2O_3/NiAl(110)$: representative series of C 1s spectra taken after CO saturation at 90 K and heating to the indicated temperatures (data acquisition at 90 K).

the observation that the dissociation activity declines much faster in this case (Fig. 30).

A detail of the dissociation process is evident from a close inspection of the C 1s emission of the molecularly adsorbed CO (*189*). As shown in Fig. 31a, the peak is resolved into two components, denoted A and B. If the fraction of the total intensity found for component B after heating to 300 K is compared with the fraction of CO finally dissociating (Fig. 30), the species giving rise to B can be regarded as a kind of dissociation precursor. The evolution of each of these two quantities as a function of the particle size is identical, i.e., each pass through a maximum at the same particle size (*189*). At 90 K, however, the relative intensity is constant: It is the heating step which causes a shift of intensity from component A to component B (i.e., an increase of the B species which is most pronounced

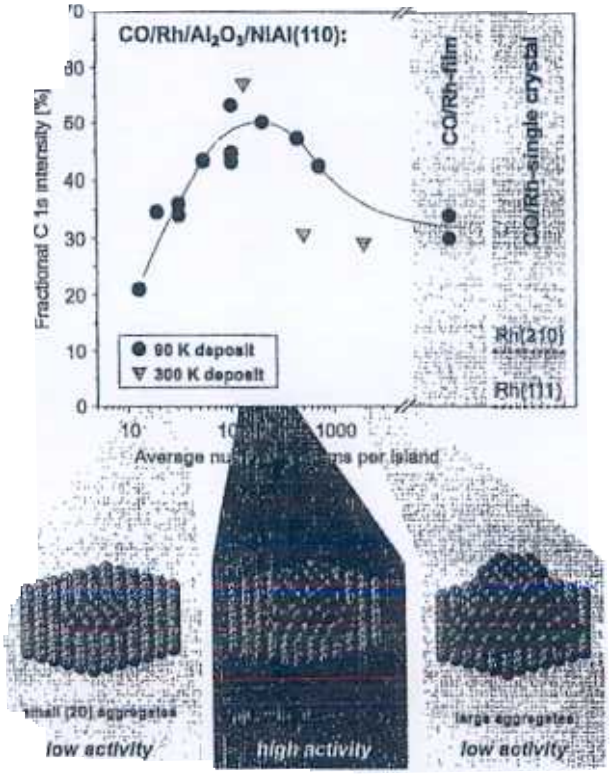

FIG. 30. CO dissociation activity on rhodium particles deposited on Al_2O_3/NiAl(110) as determined by XPS. According to Frank *et al.* (*188, 189*), the dissociation activity also passes through a maximum for the 300-K deposits, i.e., the activity decreases in the regime of small particle sizes reflecting the behavior of the 90-K deposits.

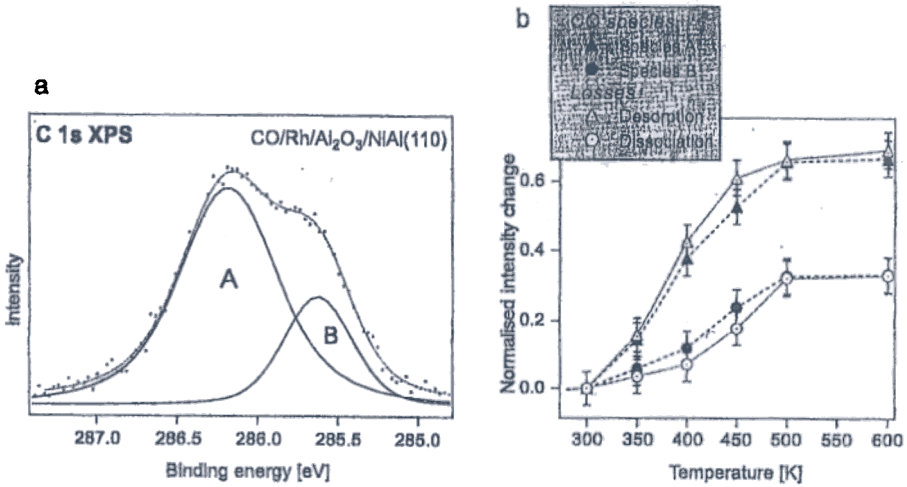

FIG. 31. (a) C 1s spectrum of CO adsorbed on rhodium particles after saturation at 90 K; (b) intensity changes for the components A and B as well as the intensity losses due to dissociation and desorption as a function of the annealing temperature (the average particle contained ~10^4 atoms).

for the medium-sized particles). This conversion is irreversible; cooling does not lead to an intensity redistribution.

The conclusion that B is indeed a dissociation precursor is additionally corroborated by the results of Fig. 31b showing the intensity changes for the A and B peaks as well as the losses which result from either desorption or dissociation (*190*). Unambiguously, the desorption curve follows the curve for component A, whereas the dissociation curve mimics the development of the component B. Unfortunately, the results allow no further statement as to the nature of the A and B species. It can be assumed, however, that the B species is associated with CO adsorbed on defects. On the basis of the fact that more highly coordinated CO species give rise to lower C 1s binding energies, it may be further speculated whether B is associated with CO in a higher coordination than the A species.

As the final example of the size-dependent properties of well-defined model systems, we review recent data for the photoinduced reaction of methane interacting with palladium aggregates supported on alumina (*194*). Figure 32 shows TDS data for CD_4 desorbing from palladium aggregates of various sizes without having been exposed to light. The variation of the maximum desorption temperature with particle size represents differences of several tens of meV in interaction energy between CH_4 and the palladium aggregates. Since we know from photoemission measurements that the density of metal states at the Fermi energy varies and that energy gaps exist for very small aggregates, it is conceivable that the dispersive molecule–surface interactions vary as the density of states at the Fermi energy varies.

In the dark, CH_4 does not dissociate in the current situation. If the system is exposed to ultraviolet light with a wavelength in the range of 5.2–6.4 eV, however, CH_4 dissociation into adsorbed CH_3 and H fragments is observed (*194*). In a characteristic way, recombinative desorption occurs at temperatures exceeding 110 K, and this desorption is clearly separated from the CH_4 molecular desorption peak. By evaluating the relative areas

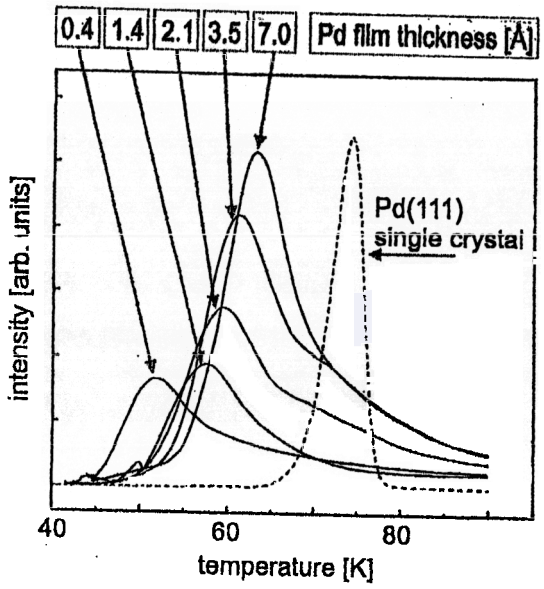

FIG. 32. Series of CD_4 TDS spectra (m/e = 20; solid curves) of palladium clusters of various sizes deposited on a thin Al_2O_3 layer epitaxially grown on NiAl(110). The sample was exposed to 0.5 liters of CD_4 at 40 K. The desorption peaks are indicative of molecular desorption, CD_4 (ads) → CD_4(g). The numbers denote the total palladium coverages as a measure of the cluster size. The dashed curve corresponds to a TDS spectrum of a Pd(111) single-crystal surface after exposure to 0.6 liters of CD_4 and is plotted with a different scale. The heating rate for the clusters was 0.5 K s^{-1} and that for the Pd(111) single crystal was 0.4 K s^{-1}.

in the TDS spectra characterizing direct and recombinative desorption, we can determine the ratio of photon-stimulated molecular desorption to photoinduced dissociation. In Fig. 33, these quantities are plotted as a function of aggregate size. The data show qualitatively that small aggregates support photodesorption, whereas photodissociation sets in for larger aggregates. In the limit of large aggregates, the behavior on Pd(111) single-crystal surfaces is approached (*195*).

Watanabe *et al.* (*195*) found that CH_4 may be photodissociated on Pd(111) at a photon energy of 6.4 eV, whereas in the gas phase this process cannot be induced at a photon energy lower than 8.4 eV (*196*). A model has been proposed in which the relevant excited state (of Rydberg character) of the CH_4 molecule is stabilized by the interaction with unoccupied states of the substrate (*197*), thus leading to a shift of the dissociation threshold to lower energy. The size dependence results from the change of the unoccupied

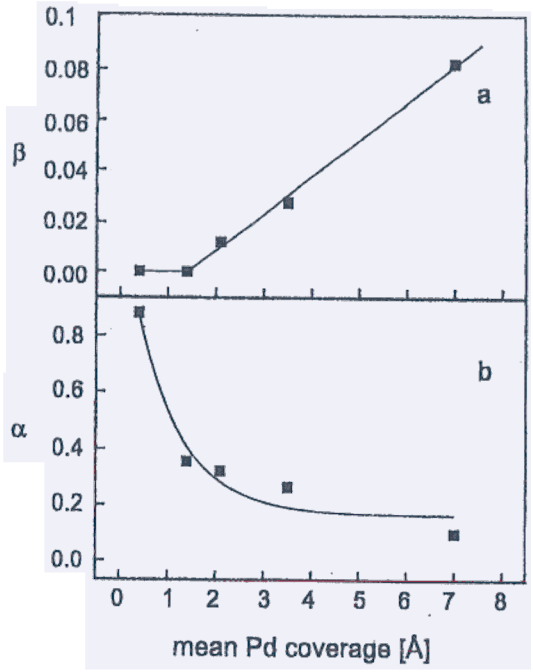

FIG. 33. (a) Plot of the CD_3H formation ratio β ($\beta = B/A_0$, where B is the integrated TDS peak area of CD_3H after irradiation and A_0 is the integrated TDS peak area of initially adsorbed CD_4 before irradiation) as a function of the total palladium coverage. (b) Plot of the CD_4 depletion ratio α ($\alpha = 1 - A/A_0$, where A_0 is the integrated peak area of CD_4 before irradiation and A is the integrated peak area of CD_4 after irradiation with 1.5×10^{19} photons/cm^2) as a function of the total palladium coverage. The total palladium coverages of 1.4, 2.1, 3.5, and 7 Å correspond to average cluster sizes of 37, 49, 65, and 73 atoms, respectively, as determined by a spot profile LEED analysis.

density of states in the aggregate with size, which for the smallest aggregates does not allow effective coupling to the CH_4 excited state. An alternative model has been proposed (*198*) which is based on the idea that the photon induces charge transfer from the CH_4 molecule to the aggregate. The energy necessary for such a process is then governed by the electron affinity of the aggregate, which varies with size and the ionization potential of CH_4. An important additional ingredient is the stabilization of the charge transfer by an image charge in the aggregate, which also varies with size. A qualitative estimate yields a threshold energy of 5 eV for dissociation, which is consistent with the currently available experimental results.

The field of investigations of chemical reactivity as a function of aggregate size is still emerging, and there are more exciting results on the horizon.

IV. Conclusions

After 30 years of surface science, which have seen an enormous development of methods and instrumentation, the field is now in a position to tackle questions of a complex nature. Naturally, metal surfaces have been the focus of attention in surface science to date, and this trend will continue. However, the complexity of problems is constantly increasing, particularly if molecular adsorbates and self-organized systems are considered. Metal oxide surfaces have received some attention in the recent past, and the study of such systems as well as more complex metal/metal-oxide composite systems has already defined a direction in surface science that promises interesting results of fundamental interest as well as of potential value for catalytic applications. It is encouraging that surface science is still a very active and productive field. Without a doubt, further impact on catalysis research can be expected in the future.

Acknowledgments

We are grateful to those colleagues whose names appear in the references. We also thank many colleagues for stimulating discussions and collaboration, especially Ralph Wichtendahl for his help in preparing the figures. The following have provided support for our work: Deutsche Forschungsgemeinschaft, Bundesministerium für Bildung und Forschung, Ministerium für Wissenschaft und Forschung des Landes Nordrhein-Westfalen, Fonds der Chemischen Industrie, German–Israeli Foundation, European Union, NEDO International Joint Research Grant on Photon and Electron Controlled Surface Processes, Hoechst Celanese, and Synetix, a member of the ICI group, through their Strategy Research Fund.

References

1. Duke, C. B. (Ed.), "Surface Science: The First Thirty Years." Elsevier, Amsterdam, 1994.
2. Ertl, G., and Freund, H.-J., *Phys. Today* **52,** 32 (1999).
3. Freund, H.-J., *Ber. Bunsenges. Phys. Chem.* **99,** 1261 (1995).
4. Bonzel, H. P., *Surf. Sci.* **68,** 236 (1977).
5. Freund, H.-J., and Umbach, E. (Eds.), "Adsorption on Ordered Surfaces of Ionic Solids and Thin Films." Springer, Heidelberg, 1993.
6. Henry, C. R., *Surf. Sci. Rep.* **31,** 231 (1998).
7. Campbell, C. T., *Surf. Sci. Rep.* **27,** 1 (1997).
8. Campbell, C. T., *Curr. Opin. Solid State Mater. Sci.* **3,** 439 (1998).
9. Freund, H.-J., Kuhlenbeck, H., and Staemmler, V., *Rep. Progr. Phys.* **59,** 283 (1996).
10. Bäumer, M., and Freund, H.-J., *Progr. Surf. Sci.* **61,** 127 (1999).
11. Goodman, D. W., *Surf. Rev. Lett.* **2,** 9 (1995).
12. Diebold, U., Pan, J.-M., and Madey, T. E., *Surf. Sci.* **331–333,** 845 (1995).
13. Freund, H.-J., *Angew. Chem. Int. Ed. Engl.* **36,** 452 (1997).
14. Poppa, H., *Catal. Rev. Sci. Eng.* **35,** 359 (1993).
15. Vurens, G. H., Salmeron, M., and Somorjai, G. A., *Progr. Surf. Sci.* **32,** 333 (1989).
16. Gunter, P. L. J., Niemantsverdriet, J. W. H., Ribeiro, F. H., and Somorjai, G. A., *Catal. Rev. Sci. Eng.* **39,** 77 (1997).

17. Bonnell, D. A., *Progr. Surf. Sci.* **57,** 187 (1998).
18. Chen, J. G., *Surf. Sci. Rep.* **30,** 1 (1997).
19. Müller, C., Uebing, C., Kottcke, M., Rath, C., Hammer, L., and Heinz, K., *Surf. Sci.* **400,** 87 (1998).
20. Wiegenstein, C. G., and Schulz, K. H., *Surf. Sci.* **396,** 284 (1998).
21. Henrich, V. E., and Cox, P. A., "The Surface Science of Metal Oxides." Cambridge Univ. Press, Cambridge, UK, 1994.
22. Heiz, U., and Schneider, W.-D., *in* "Cluster–Solid Surface Interaction" (K.-H. Meiwes-Broer, Ed.). Springer, Berlin, 1999.
23. Gates, B. C., Guczi, L., and Knözinger, H., (Eds.), "Metal Clusters in Catalysis." Elsevier, Amsterdam, 1986.
24. Knözinger, H., *Catal. Today* **32,** 71 (1996).
25. Zecchina, A., Scarano, D., Bordiga, S., Ricchiardi, G., Spoto, G., and Geobaldo, F., *Catal. Today* **27,** 403 (1996).
26. Seiferth, O., Wolter, K., Dillmann, B., Klivenyi, G., Freund, H.-J., Scarano, D., and Zecchina, A., *Surf. Sci.* **421,** 176 (1999).
27. Hävecker, M., Knop-Gericke, A., Schedel-Niedrig, T., and Schlögl, R., *Angew. Chem. Int. Ed. Engl.* **37,** 1939 (1998).
28. Diebold, U., Anderson, J. F., Ng, K.-O., and Vanderbilt, D., *Phys. Rev. Lett.* **77,** 1322 (1996).
29. Murray, P. W., Leibsle, F. M., Muryn, C. A., Fisher, H. J., Flipse, C. F. J., and Thornton, G., *Phys. Rev. Lett.* **72,** 689 (1994).
30. Murray, P. W., Condon, N. G., and Thornton, G., *Phys. Rev. B* **51,** 10989 (1995).
31. Onishi, H., and Iwasawa, Y., *Surf. Sci.* **313,** L783 (1994).
32. Onishi, H., and Iwasawa, Y., *Chem. Phys. Lett.* **226,** 111 (1994).
33. Onishi, H., Fukui, K., and Iwasawa, Y., *Bull. Chem. Soc. Jpn.* **68,** 2447 (1995).
34. Onishi, H., and Iwasawa, Y., *Phys. Rev. Lett.* **76,** 791 (1996).
35. Charlton, G., Howes, P. B., Nicklin, C. L., Steadman, P., Taylor, J. S. G., Muryn, C. A., Harte, S. P., Mercer, J., McGrath, R., Norman, D., Turner, T. S., and Thornton, G., *Phys. Rev. Lett.* **78,** 495 (1997).
36. Renaud, G., *Surf. Sci. Rep.* **32,** 1 (1998).
37. Tasker, P. W., *Adv. Ceram.* **10,** 176 (1984).
38. Mackrodt, W. C., Davey, R. J., Black, I. N., and Docherty, R., *J. Cryst. Growth* **82,** 441 (1987).
39. Noguera, C., "Physics and Chemistry at Oxide Surfaces." University Press, Cambridge, UK, 1996.
40. Guénard, P., Renaud, G., Barbier, A., and Gantier-Soyer, M., *Surf. Rev. Lett.* **5,** 321 (1998).
41. Rohr, F., Bäumer, M., Freund, H.-J., Mejias, J. A., Staemmler, V., Müller, S., Hammer, L., and Heinz, K., *Surf. Sci.* **372,** L291 (1997).
42. Rohr, R., Bäumer, M., Freund, H.-J., Mejias, J. A., Staemmler, V., Muller, S., Hammer, L., and Heinz, K., *Surf. Sci.* **389,** 391 (1997).
43. Weiss, W., *Surf. Sci.* **377–379,** 943 (1997).
44. Manassidis, L., and Gillan, M. J., *Surf. Sci.* **285,** L517 (1993).
45. Manassidis, L., and Gillan, M. J., *J. Am. Ceram. Soc.* **77,** 335 (1994).
46. Rebhein, C., Harrison, N. M., and Wander, A., *Phys. Rev. B* **54,** 14066 (1996).
47. Wang, X.-G., Weiss, W., Shaikhutdinov, S. K., Ritter, M., Petersen, M., Wagner, F., Schloegl, R., and Scheffler, M., *Phys. Rev. Lett.* **81,** 1038 (1998).
48. Refson, K., Wogelius, R. A., Fraser, D. G., Payne, M. C., Lee, M. H., and Milman, V., *Phys. Rev. B* **52,** 10823 (1995).

49. Birkenheuer, U., Boettger, J. C., and Rösch, N., *J. Chem. Phys.* **100,** 6826 (1994).
50. Heinz, K., *Surf. Sci.* **299,** 433 (1984).
51. Harrison, N. M., Wang, X.-G., Muscat, M., and Scheffler, M., *Faraday Disc.* **114,** 305 (1999).
52. Schmalzried, H., "Chemical Kinetics of Solids." VCH, Weinheim, 1995.
53. Wolf, D., *Phys. Rev. Lett.* **68,** 3315 (1992).
54. Barbier, A., and Renaud, G., *Surf. Sci.* **392,** L15 (1997).
55. Cappus, D., Xu, C., Ehrlich, D., Dillmann, B., Ventrice Jr., C. A., Al-Shamery, K., Kuhlenbeck, H., and Freund, H.-J., *Chem. Phys.* **177,** 533 (1993).
56. Rohr, F., Wirth, K., Libuda, J., Cappus, D., Bäumer, M., and Freund, H.-J., *Surf. Sci.* **315,** L977 (1994).
57. Barbier, A., Proceedings of the 1st International Workshop on Oxide Surfaces, Elmau, Germany, 1999.
58. Lacman, R., *Colloq. Int. CNRS* **152,** 195 (1965).
59. Ventrice, C. A., Jr., Bertrams, T., Hannemann, H., Brodde, A., and Neddermeyer, H., *Phys. Rev. B* **49,** 1773 (1994).
60. Barbier, A., Mocuta, C., Kuhlenbeck, H., Peters, K., Richter, B., and Renaud, G., to be published.
61. Casey, W. H., Westrich, H. R., and Arnold, G. W., *Geochim. Cosmochim. Acta* **53,** 2795 (1988).
62. Papp, H., and Egersdörfer, B., personal communication.
63. Egersdörfer, B., PhD thesis, Ruhr-Universität, Bochum, Germany, 1993.
64. Fripiat, J. G., Lucas, A. A., André, J. M., and Derouane, E. G., *Chem. Phys.* **21,** 101 (1977).
65. Henzler, M., and Göpel, W., "Oberflächenphysik des Festkörpers." Teubner-Verlag, Stuttgart, 1991.
66. Neyman, K. M., Pacchioni, G., and Rösch, N., *in* "Recent Developments and Applications of Modern Density Functional Theory and Computational Chemistry" (J. M. Seminario, Ed.), p. 569. Elsevier, Amsterdam, 1996.
67. Pöhlchen, M., and Staemmler, V., *J. Chem. Phys.* **97,** 2583 (1992).
68. Pacchioni, G., and Bagus, P. S., *in* "Adsorption on Ordered Surfaces of Ionic Solids and Thin Films" (H.-J. Freund and E. Umbach, Eds.), Vol. 33, p. 180. Springer-Verlag, Berlin, 1993.
69. Nygren, M. A., and Pettersson, L. G. M., *J. Chem. Phys.* **105,** 9339 (1996).
70. Wichtendahl, R., Rodriguez-Rodrigo, M., Härtel, U., Kuhlenbeck, H., and Freund, H.-J., *Phys. Stat. Sol. A* **173,** 93 (1999).
71. Heidberg, J., Kandel, M., Meine, D., and Wildt, U., *Surf. Sci.* **333,** 1467 (1995).
72. Gerlach, R., Glebov, A., Lange, G., Toennies, J. P., and Weiss, W., *Surf. Sci.* **331–333,** 1490 (1995).
73. Wichtendahl, R., PhD thesis, Freie Universität, Berlin, 1999.
74. Stirniman, M. J., Huang, C., Smith, R. C., Joyce, J. A., and Kay, B. D., *J. Chem. Phys.* **105,** 1295 (1996).
75. Xu, C., and Goodman, D. W., *Chem. Phys. Lett.* **L65,** 341 (1997).
76. Libuda, J., Frank, M., Sandell, A., Andersson, S., Brühwiler, P. A., Bäumer, M., Mårtensson, N., and Freund, H.-J., *Surf. Sci.* **384,** 106 (1997).
77. Valden, M., and Goodman, D. W., *Science* **281,** 1647 (1998).
78. Hemminger, J., personal communication.
79. Jaeger, R. M., Kuhlenbeck, H., Freund, H.-J., Wuttig, M., Hoffmann, W., Franchy, R., and Ibach, H., *Surf. Sci.* **259,** 235 (1991).
80. Engquist, I., and Liedberg, B., *J. Phys. Chem.* **100,** 20089 (1996).
81. Knözinger, H., and Ratnasaniy, P., *Catal. Rev. Sci. Eng.* **17,** 31 (1978).

82. Ehrlich, D., PhD. Ruhr-Universität, thesis, Bochum, Germany, 1995.
83. Kuhlenbeck, H., Xu, C., Dillmann, B., Haßel, M., Adam, B., Ehrlich, D., Wohlrab, S., Freund, H.-J., Ditzinger, U. A., Neddermeyer, H., Neuber, M., and Neumann, M., *Ber. Bunsenges. Phys. Chem.* **96,** 15 (1992).
84. Xu, C., Dillmann, B., Kuhlenbeck, H., and Freund, H.-J., *Phys. Rev. Lett.* **67,** 3551 (1991).
85. Xu, C., Haßel, M., Kuhlenbeck, H., and Freund, H.-J., *Surf. Sci.* **258,** 23 (1991).
86. Hemmerich, I., Rohr, F., Seiferth, O., Dillmann, B., and Freund, H.-J., *Z. Phys. Chem.* **202,** 31 (1997).
87. Thüne, P. C., and Niemantsverdriet, J. W., *Israel. J. Chem.* **38,** 385 (1998).
88. Menges, M., Baumeister, B., Al-Shamery, K., Freund, H.-J., Fischer, C., and Andresen, P., *J. Chem. Phys.* **101**(4), 3318 (1994).
89. Beauport, I., Al-Shamery, K., and Freund, H.-J., *Chem. Phys. Lett.* **256,** 641 (1996).
90. Klüner, T., Freund, H.-J., Staemmler, V., and Kosloff, R., *Phys. Rev. Lett.* **80,** 5208 (1998).
91. Al-Shamery, K., *Appl. Phys. A* **63,** 509 (1996).
92. Wovchko, E. A., and Yates, J. T., Jr., *Langmuir* **15,** 3506 (1999).
93. Wu, M. C., and Møller, P. J., *Surf. Sci.* **221,** 250 (1989).
94. Möller, P. J., and Wu, M. C., *Surf. Sci.* **224,** 265 (1989).
95. Wu, M. C., and Møller, P. J., *Surf. Sci.* **235,** 228 (1990).
96. Møller, P. J., and Nerlov, J., *Surf. Sci.* **307–309,** 591 (1993).
97. Murray, P. W., Shen, J., Condon, N. G., Peng, S. J., and Thornton, G., *Surf. Sci.* **380,** L455 (1997).
98. Stone, P., Bennett, R. A., and Bowker, M., *New J. Phys.* **1,** 8 (1989-1999).
99. Diebold, U., Proceedings of the 1st International Workshop on Oxide Surfaces, Elmau, Germany, 1999.
100. Xu, X., Vesecky, S. M., and Goodman, D. W., *Science* **258,** 788 (1992).
101. Schröder, T., Adelt, M., Richter, B., Naschitzki, M., Bäumer, M., and Freund, H.-J., submitted for publication.
102. Gunthaner, F. J., Gunthaner, P. J., Vasquez, R. P., Lewis, B. F., Maserjian, J., and Madhukar, A., *J. Vac. Sci. Technol.* **16,** 1443 (1979).
103. Libuda, J., Winkelmann, F., Bäumer, M., Freund, H.-J., Bertrams, T., Neddermeyer, H., and Müller, K., *Surf. Sci.* **318,** 61 (1994).
104. Stempel, S., Bäumer, M., and Freund, H.-J., *Surf. Sci.* **402–404,** 424 (1998).
105. Heemeier, M., PhD thesis, Freie Universität, Berlin, manuscript in preparation.
106. Linderoth, T. R., Horch, S., Lænsgaard, E., Stensgaard, I., and Besenbacher, F., *Surf. Sci.* **404,** 308 (1998).
107. Ernst, N., Duncombe, B., Bozdech, G., Naschitzki, M., and Freund, H.-J., *Ultramicroscopy* **79,** 231 (1999).
108. Piednoir, A., Pernot, E., Granjeand, S., Humbert, A., Chapon, C., and Henry, C. R., *Surf. Sci.* **391,** 19 (1997).
109. Hansen, K. H., Worren, T., Stempel, S., Lægsgaard, E., Bäumer, M., Freund, H.-J., Besenbacher, F., and Stensgaard, I., submitted for publication.
110. Methfessel, M., Hennig, D., and Scheffler, M., *Phys. Rev. B* **46,** 4816 (1992).
111. Bogicevic, A., and Jennison, D. R., *Phys. Rev. Lett.* **82,** 4050 (1999).
112. Klimenkov, M., Nepijko, S., Kuhlenbeck, H., Bäumer, M., Schlögl, R., and Freund, H.-J., *Surf. Sci.* **391,** 27 (1997).
113. Klimenkov, M., Nepijko, S., Kuhlenbeck, H., and Freund, H.-J., *Surf. Sci.* **385,** 66 (1997).
114. Nepijko, S., Klimenkov, M., Kuhlenbeck, H., Zemlyanov, D., Herein, D., Schlögl, R., and Freund, H.-J., *Surf. Sci.* **413,** 192 (1998).
115. Nepijko, S. A., Klimenkov, M., Adelt, M., Kuhlenbeck, H., Schlögl, R., and Freund, H.-J., *Langmuir* **15,** 5309 (1999).

116. Rupprechter, G., Eppler, A. S., and Somorjai, G. A., *in* "Electron Microscopy 1998" (H. A. C. Benavides and M. J. Yacaman, Eds.), Vol. 2, p. 369. Institute of Physics Publishing, Philadelphia, 1998.
117. Eppler, A. S., Rupprechter, G., Guczi, L., and Somorjai, G. A., *J. Phys. Chem. B* **101,** 9973 (1997).
118. Wong, K., Johansson, S., and Kasemo, B., *Faraday Disc.* **105,** 237 (1996).
119. Jacobs, P. W., Ribero, F. H., Somorjai, G. A., and Wind, S. J., *Catal. Lett.* **37,** 131 (1996).
120. Gotschy, W., Vonmetz, K., Leitner, A., and Aussenegg, F. R., *Appl. Phys. B* **63,** 381 (1996).
121. Cerrina, F., and Marrian, C., *MRS Bull.* **21,** 56 (1996).
122. Fischer, P. B., and Chou, S. Y., *Appl. Phys. Lett.* **62,** 2989 (1993).
123. Queeney, K. T., Pang, S., and Friend, C. M., *J. Chem. Phys.* **109,** 8058 (1998).
124. Queeney, K. T., and Friend, C. M., to be published.
125. Leisenberger, F. P., Surnev, S., Vitali, L., Ramsey, M. G., and Netzer, F. P., *J. Vac. Sci. Technol. A* **17,** 1743 (1999).
126. Grant, J. L., Fryberger, T. B., and Stair, P. C., *Surf. Sci.* **239,** 127 (1990).
127. Schmid, G., (Ed.), "Clusters and Colloids: From Theory to Applications." VCH, Weinheim, 1994.
128. Ekardt, W. (Ed.), "Metal Clusters." Wiley, Chichester, UK, 1999.
129. de Biani, F. F., Femoni, C., Iapalucci, M. C., Longoni, G., Zanello, P., and Ceriotti, A., *Inorg. Chem.* **38,** 3721 (1999).
130. Johnson, B. F. G. (Ed.), "Transition Metal Clusters." Wiley, Chichester, UK, 1980.
131. Wertheim, G. K., DiCenzo, S. B., and Buchanan, D. N. E., *Phys. Rev. B* **33,** 5384 (1986).
132. Sandell, A., Libuda, J., Brühwiler, P., Andersson, S., Maxwell, A., Bäumer, M., Mårtensson, N., and Freund, H.-J., *J. Electron Spectrosc. Relat. Phenom.* **76,** 301 (1995).
133. Unwin, R., and Bradshaw, A. M., *Chem. Phys. Lett.* **58,** 58 (1978).
134. Wertheim, G. K., *Z. Phys. D* **12,** 319 (1989).
135. Lee, S.-T., Apai, G., Mason, M. G., Benbow, R., and Hurych, Z., *Phys. Rev. B* **23,** 505 (1981).
136. de Gouveia, V., Bellamy, B., Hadj Romdhane, Y., Mason, A., and Che, M., *Z. Phys. D* **12,** 587 (1989).
137. Kuhrt, C., and Harsdorff, M., *Surf. Sci.* **245,** 173 (1991).
138. Sandell, A., Libuda, J., Brühwiler, P. A., Andersson, S., Maxwell, A. J., Bäumer, M., Mårtensson, N., and Freund, H.-J., *J. Vac. Sci. Technol. A* **14,** 1546 (1996).
139. Goodman, D. W., *J. Vac. Sci. Technol. A* **14,** 1526 (1996).
140. Sandell, A., Libuda, J., Brühwiler, P. A., Andersson, S., Bäumer, M., Maxwell, A. J., Mårtensson, N., and Freund, H.-J., *Phys. Rev. B* **55,** 7233 (1997).
141. Frederick, B. B., Apai, G., and Rhodin, T. N., *J. Am. Chem. Soc.* **109,** 4797 (1987).
142. Wertheim, G. K., *Z. Phys. B* **66,** 53 (1987).
143. Mason, M. G., *Phys. Rev. B* **27,** 748 (1983).
144. Cini, M., de Crescenzi, M., Patella, F., Motta, N., Sastry, M., Rochet, F., Pasquali, R., Balzarotti, A., and Verdozzi, C., *Phys. Rev. B* **41,** 5685 (1990).
145. Vijayakrishnan, V., and Rao, C. N. R., *Surf. Sci. Lett.* **255,** L516 (1991).
146. Jirka, I., *Surf. Sci.* **232,** 307 (1990).
147. Wertheim, G. K., CiCenzo, S. B., and Youngquist, S. E., *Phys. Rev. Lett.* **51,** 2310 (1983).
148. DiCenzo, S. B., and Wertheim, G. K., *Comments Solid State Phys.* **11,** 203 (1985).
149. Häberlen, O. D., Chung, S.-C., Stener, M., and Rösch, N., *J. Chem. Phys.* **106,** 5189 (1997).
150. Björneholm, O., Nilsson, A., Zdansky, E. O. F., Sandell, A., Hernnäs, B., Tillborg, H., Anderson, J. N., and Mårtensson, N., *Phys. Rev. B* **46,** 10353 (1992).
151. Nilsson, A., Björneholm, O., Zdansky, E. O. F., Tillborg, H., Mårtensson, N., Andersen, J. N., and Nyholm, R., *Chem. Phys. Lett.* **197,** 1892 (1992).

152. Rainer, D. R., and Goodman, D. W., *in* "NATO ASI" (G. Pacchioni and R. M. Lambert, Eds.), Vol. 331, p. 27. Kluwer, Dordrecht, 1997.
153. Meiwes-Broer, K. H., *Phys. Bl.* **55,** 21 (1999).
154. Adelt, M., Nepijko, S., Drachsel, W., and Freund, H.-J., *Chem. Phys. Lett.* **291,** 425 (1998).
155. Dormann, J. L., and Fiorani, D. (Eds.), "Magnetic Properties of Fine Particles." North-Holland, Amsterdam, 1992.
156. Hill, T., Mozaffari-Afshar, M., Schmidt, J., Risse, T., Stempel, S., Heemeier, M., and Freund, H.-J., *Chem. Phys. Lett.* **292,** 524 (1998).
157. Hill, T., Stempel, S., Risse, T., Bäumer, M., and Freund, H.-J., *J. Magn. Magn. Mater.* **198/199,** 354 (1999).
158. Hill, T., Mozaffari-Afshar, M., Schmidt, J., Risse, T., and Freund, H.-J., *Surf. Sci.* **429,** 246 (1999).
159. Risse, T., Hill, T., Mozaffari-Afshar, M., and Freund, H.-J., submitted for publication.
160. Evans, J., Hayden, B., Mosselman, F., and Murray, A., *Surf. Sci.* **279,** L159 (1992).
161. Evans, J., Hayden, B., Mosselman, F., and Murray, A., *Surf. Sci.* **301,** 61 (1994).
162. Wolter, K., Seiferth, O., Kuhlenbeck, H., Bäumer, M., and Freund, H.-J., *Surf. Sci.* **399,** 190 (1998).
163. Frank, M., Kühnemuth, R., Bäumer, M., and Freund, H.-J., *Surf. Sci.* **427/428,** 288 (1999).
164. Frank, M., Kühnemuth, R., Bäumer, M., and Freund, H.-J. submitted for publication.
165. Yates, J. T., Jr., Duncan, T. M., Worley, S. D., and Vaughan, R. W., *J. Chem. Phys.* **70,** 1219 (1979).
166. Basu, P., Panayotov, D., and Yates, J. T., Jr., *J. Am. Chem. Soc.* **110,** 2074 (1988).
167. Solymosi, F., and Knözinger, H., *J. Chem. Soc. Faraday Trans.* **86,** 389 (1990).
168. Berkó, A., and Solymosi, F., *J. Catal.* **183,** 91 (1999).
169. Bäumer, M., Frank, M., Heemeier, M., Kühnemuth, R., Stempel, S., and Freund, H.-J., to be published.
170. Jaeger, R. M., Libuda, J., Bäumer, M., Homann, K., Kuhlenbeck, H., and Freund, H.-J., *J. Electron Spectrosc. Relat. Phenom.* **64/65,** 217 (1993).
171. Mineva, T., and Russo, N., personal communication.
172. Uvdal, P., Karlsson, P.-A., Nyberg, C., Andersson, S., and Richardson, N. V., *Surf. Sci.* **202,** 167 (1988).
173. Giessel, T., Schaff, O., Hirschmugl, C. J., Fernandez, V., Schindler, K. M., Theobald, A., Bao, S., Lindsay, R., Berndt, W., Bradshaw, A. M., Baddeley, C., Lee, A. F., Lambert, R. M., and Woodruff, D. P., *Surf. Sci.* **406,** 90 (1998).
174. Kisters, G., Chen, J. G., Lehwald, S., and Ibach, H., *Surf. Sci.* **245,** 65 (1991).
175. Lauterbach, J., Boyle, R. W., Schick, M., Mitchell, W. J., Meng, B., and Weinberg, W. H., *Surf. Sci.* **350,** 32 (1996).
176. Solymosi, F., Novák, É., and Molnár, A., *J. Phys. Chem.* **94,** 7250 (1990).
177. Voskobojnikov, T. W., Shpiro, E. S., Landmesser, H., Jaeger, N. I., and Schulz-Ekloff, G., *J. Mol. Catal. A Chem.* **104,** 299 (1996).
178. De La Cruz, C., and Sheppard, N., *J. Chem. Soc. Faraday Trans.* **93,** 3569 (1997).
179. Hansen, K. H., Stempel, S., Lægsgaard, E., Besenbacher, F., and Stensgaard, I., personal communication.
180. Conrad, H., Ertl, G., and Küppers, J., *Surf. Sci.* **76,** 323 (1978).
181. Haruta, M., *Catal. Today* **36,** 153 (1997).
182. Piccolo, L., Becker, C., and Henry, C. R., *Eur. Phys. J.* **8** (1999).
183. Zhdanov, V. P., and Kasemo, B., *Phys. Rev. B* **55,** 4105 (1997).
184. Persson, H., Thormählen, P., Zhdanov, V. P., and Kasemo, B., *Catal. Today* **53,** 273 (1999).
185. Vanolli, F., Heiz, U., and Schneider, W.-D., *Chem. Phys. Lett.* **277,** 527 (1997).

186. Heiz, U., Sanchez, A., Abbet, S., and Schneider, W.-D., *J. Am. Chem. Soc.* **121,** 3214 (1999).
187. Richter, B., Wilkes, J., Wichtendahl, R., Kuhlenbeck, H., and Freund, H.-J., unpublished manuscript.
188. Frank, M., Andersson, S., Libuda, J., Stempel, S., Sandell, A., Brena, B., Giertz, A., Bruhwiler, P. A., Bäumer, M., Mårtensson, N., and Freund, H.-J., *Chem. Phys. Lett.* **279,** 92 (1997).
189. Andersson, S., Frank, M., Sandell, A., Giertz, A., Brena, B., Brühwiler, P. A., Mårtensson, N., Libuda, J., Bäumer, M., and Freund, H.-J., *J. Chem. Phys.* **108,** 2967 (1998).
190. Andersson, S., Frank, M., Sandell, A., Libuda, J., Brena, B., Giertz, A., Brühwiler, P. A., Bäumer, M., Mårtensson, N., and Freund, H.-J., *Vacuum* **49,** 167 (1998).
191. Irion, M. P., personal communication.
192. Yates, J. T., Williams, E. D., and Weinberg, W.H., *Surf. Sci.* **91,** 562 (1980).
193. Rebholz, M., Prins, R., and Kruse, N., *Surf. Sci.* **259,** L791 (1991).
194. Watanabe, K., Matsumoo, Y., Kampling, M., Al-Shamery, K., and Freund, H.-J., *Angew. Chem. Int. Ed.* **38,** 2192 (1999).
195. Watanabe, K., and Matsumoto, Y., *Surf. Sci.* **390,** 250 (1997).
196. Herzberg, G., "Molecular Spectra and Molecular Structure." Van Nostrand, New York, 1966.
197. Akinaga, Y., Taketsugu, T., and Hirao, T., *J. Chem. Phys.* **107,** 415 (1997).
198. Jennison, D. R., personal communication.
199. Heidberg, J., Redlich, B., and Wetter, D., *Ber. Bunsenges. Phys. Chem.* **99,** 1333 (1995).